Functional redundancy of WDR31 with GTPase-activating proteins ELMOD and RP2 in regulating IFT trains via BBSome

Sebiha Cevik[1], Xiaoyu Peng[2], Tina Beyer[3], Mustafa S. Pir[1], Ferhan Yenisert[1], Franziska Woerz[4], Felix Hoffmann[3], Betul Altunkaynak[1], Betul Pir[1], Karsten Boldt[3], Asli Karaman[5], Miray Cakiroglu[5], S. Sadik Oner[4,5], Ying Cao[2], Marius Ueffing[3], Oktay I. Kaplan[1]†

1- Rare Disease Laboratory, School of Life and Natural Sciences, Abdullah Gul University, Kayseri, Turkey

2- School of Life Sciences and Technology, Tongji University, Shanghai 200092, China

3- Institute for Ophthalmic Research, Centre for Ophthalmology, University of Tuebingen, Elfriede-Aulhorn-Strasse 7, D-72076 Tuebingen, Germany.

4- Goztepe Prof. Dr. Suleyman Yalcin City Hospital, Istanbul, Turkey

5- Science and Advanced Technology Application and Research Center, Istanbul Medeniyet University, Istanbul

† Correspondence to oktay.kaplan@agu.edu.tr

Abstract

The correct intraflagellar transport (IFT) assembly at the ciliary base and the IFT turnaround at the ciliary tip are key for the IFT to perform its function, but we still have poor understanding about how these processes are regulated. Here, we identify WDR31 as a new ciliary protein, and analysis from zebrafish and *Caenorhabditis elegans* reveals the role of *WDR31* in regulating the cilia morphology. We find that loss of WDR-31 together with RP-2 and ELMD-1 (the sole ortholog ELMOD1-3) results in ciliary accumulations of IFT Complex B components and KIF17 kinesin, with fewer IFT/BBSome particles traveling along cilia in both anterograde and retrograde directions, suggesting that the IFT/BBSome entry into cilia and exit from cilia are impacted. Furthermore, anterograde IFT in the middle segment travel at increased speed in *wdr-31;rpi-2;elmd-1*. Remarkably, a non-ciliary protein leaks into cilia of *wdr-31;rpi-2;elmd-1* possible due to IFT defects. This work reveals WDR31-RP-2-ELMD-1 as IFT and BBSome trafficking regulators.

Introduction

Cilia are structurally and functionally distinct cellular projections, consisting of a microtubule-based axoneme extending from a centriole-derived basal body anchored at the plasma membrane. Cilia consist of multiple sub-compartments (basal body, transition zone, and ciliary tip) that display different protein compositions and structure (Blacque and Sanders, 2014; Rosenbaum and Witman, 2002; Satir and Christensen, 2007). Motile cilia mediate the movement of unicellular organisms such as *Chlamydomonas reinhardtii* or are involved in fluid movement across a tissue surface (Silflow and Lefebvre, 2001; Sleigh, 1989). Non-motile cilia, also known as primary cilia, possess mechanosensory, chemosensory, and osmosensory functions, and coordinate a range of extrinsic signaling pathways involved in cellular behavior, tissue development, and homeostasis such as those mediated by Hedgehog (Hh), Wnt, and receptor tyrosine kinase ligands (e.g. PDGFα) (Anvarian et al., 2019; Bloodgood, 2009; Nachury, 2014; Scholey, 2007).

The relation between cilia and human disorders has led to a greater understanding of their importance for human health. Both motile and primary cilia have been linked to the heterogeneous class of diseases known as ciliopathies, including Joubert Syndrome, Meckel Syndrome (MKS), and Nephronophthisis (NPHP). Owing to the presence of cilia on most cell types, ciliary defects result in varying multiorgan phenotypes such as kidney defects, retinitis pigmentosa, pancreatic cysts, hearing loss, congenital heart disease, and polydactyly (Reiter and Leroux, 2017; Wheway et al., 2019).

Over the last twenty years, there has been a large effort to reveal the molecular composition of cilia and its sub-compartments using several independent approaches, including clinical genomics, proteomics, functional genomics, and bioinformatics (Arnaiz et al., 2009; Avidor-Reiss et al.,

2004; Blacque et al., 2005; Breslow et al., 2018; Choksi et al., 2014; Jensen et al., 2016; Lambacher et al., 2016; Li et al., 2004; Mick et al., 2015; Piasecki et al., 2010; Ruiz García et al., 2019; Shaheen et al., 2016; Shamseldin et al., 2020; Sigg et al., 2017; UK10K Rare Diseases Group et al., 2016; van Dam et al., 2019). Many proteins that make up the cilium, as well as many proteins that regulate cilia biology, have been identified. These collective efforts have resulted in the identification of 302 genes that are certain to be involved in cilia biogenesis, as well as over 180 ciliopathy genes. CiliaCarta estimates the total number of the ciliary genes to be about 1200 genes, implying that many more ciliary proteins and ciliopathy genes are yet to be discovered. Indeed, the genetic diagnosis of many ciliopathy disorders is still unknown (Shamseldin et al., 2020, 2020; SYSCILIA Study Group et al., 2013; van Dam et al., 2019; Wheway et al., 2019).

Structural components of cilia and cilia cargos must be transported to cilia in order to construct and sustain cilia, and mutations in genes involved in ciliary trafficking are commonly seen in ciliopathies. Cilia has a one-of-a-kind protein delivery system called intraflagellar transport (IFT). IFT is made up of multisubunit protein complexes that travel bidirectionally along the cilia. The IFT complex contains two sub-complexes, IFT-A and IFT-B, consisting of 6 and 16 protein subunits, respectively (Prevo et al., 2017). The IFT-B sub-complex and Kinesin-2 motors mediate the motility of IFT and IFT cargos from the base of the cilia to the tip of the cilia (anterograde IFT), while the IFT-A sub-complex and the cytoplasmic dynein-2 motor facilitate the retrograde IFT transport (from the cilia tip to the base of the cilia) (Blacque, 2008; Rosenbaum and Witman, 2002). The IFT-A is involved in the transport of certain membrane proteins into cilia (Lee et al., 2008; Liem et al., 2012; Mukhopadhyay et al., 2010). Mutations in genes encoding IFT components lead to defects in cilia formation in all examined organisms, indicating the importance of IFT for cilia assembly (Pazour et al., 2000; Prevo et al., 2017).

Bardet–Biedl syndrome (BBS) was classified as a ciliopathy in 2003, and eight of the highly conserved Bardet-Biedl syndrome proteins (BBS1, BBS2, BBS4, BBS5, BBS7, BBS8, BBS9, and BBIP10) establish a stable protein complex called the BBSome that undergoes IFT. Work from a range of organisms implicates the BBSome in a variety of cilia related process including acting as a cargo adaptor for removing proteins from cilia and as a regulator of the assembly and stability of IFT trains (Ansley et al., 2003; Lechtreck et al., 2009; Loktev et al., 2008; Nachury et al., 2007; Nozaki et al., 2019; Ou et al., 2007, 2005; Wei et al., 2012; Williams et al., 2014; Xu et al., 2015; Ye et al., 2018). For example, in the nematode *C. elegans* mutants lacking *bbs-7* or *bbs-8*, detachment of IFT-A and IFT-B in the amphid cilia was reported in the anterograde direction (Ou et al., 2005). Analysis with a hypomorphic mutant (*bbs-1*) revealed that BBSome is involved in attaching IFT-B components to the retrograde IFT machinery at the ciliary tips in the channel cilia of *C. elegans* (Wei et al., 2012). Though it is known that the BBSome governs the IFT assembly and returns of IFT from the cilia, we do not yet know which additional regulators control IFT assembly at the ciliary base and IFT turnaround at the ciliary tip.

To identify new IFT regulators, we focused on our single-cell RNA-seq data that compared expression profiles of ciliated cells with those of non-ciliated cells in the nematode *C. elegans,* and this work revealed novel cilia genes and potential IFT regulators, including *WDR31* (manuscript in preparation). Our gene discovery approach in combination with the use of *in vivo* IFT microscopy analysis identified *WDR31* (WD repeat domain 31) and two GTPase activating proteins (GAPs) as IFT regulators that facilitate the ciliary entry of IFT complex. Our work from Zebrafish and *C. elegans* provides significant insight into the function of WDR31 in cilia biogenesis. First, our work from *C. elegans* revealed that WDR-31 functions redundantly with two GTPase activating proteins (GAPs) ELMD-1 (the sole ortholog of the human ELMOD proteins)

and RPI-2 (human retinitis pigmentosa 2 orthologue) to control the cilia morphology. Second, knocking out *wdr-31* along with *elmd-1* or *elmd-1;rpi-2* causes IFT trafficking to be disrupted, resulting in ciliary tip accumulations of IFT-B components and the OSM-3/KIF17 motor, as well as significantly reduced BBSome recruitment to cilia. Third, fewer IFT/BBSome particles travel along cilia in both anterograde and retrograde directions in *wdr-31;rpi-2;elmd-1* triple mutants, indicating that the IFT/BBSome entry into and exit from cilia is affected. Third, anterograde IFT in the middle segment moves faster in *wdr-31;rpi-2;elmd-1*. Finally, TRAM-1, a non-ciliary membrane protein, penetrates *wdr-31;rpi-2;elmd-1* cilia. Taken together, this work identifies WDR31 and two GAP proteins (ELMOD and RP2) as regulators for IFT and BBSome trafficking.

Material and Methods

C. elegans strains, maintenance and genetic crossing

For strain maintenance and genetic crosses, a standard procedure was followed, as described by Sidney Brenner in 1974 (Brenner, 1974). After genetic cross with a marker to generate single, double and triple mutants, we used the PCR strategy to trace the mutations in following mutants: *wdr-31(T05A8.5)(tm10423)II.; wdr-31(tur003)II.; wdr-31(syb1568)II.; nphp-4(tm925)V.; mks-6(gk674)I.; elmd-1(syb630) III.; RB1550 rpi-2(K08D12.2)(ok1863) IV.*; and *bbs-8(nx77) V*. Primers can be found in Table S1.

Lipophilic fluorescent dye-uptake assay and rescue analysis

Healthy mixed-staged animals were collected using M9 buffer (3 g/L KH2PO4, 6 g/L Na2HPO4, 5 g/L NaCl, 1 mM MgSO4), centrifuged for 1 minute at 2000 rpm, and washed twice with M9 buffer to remove any bacterial contaminations. Worms were incubated for 45-60 minutes at room temperature in an M9 buffer containing lipophilic dye (1:200 dilution in M9, Invitrogen™

Vybrant™ DiI Cell-Labeling Solution) (Herman and Hedgecock, 1990). The worms were then washed twice with M9 before being moved to a new NGM plate. Wild type was always included in Dye filling assay, and the dye uptake control for the wild type was performed under a stereotype fluorescence microscope, followed by imaging with the fluorescence upright microscope. For the rescue experiment, *N2;turEx24[arl-13p::GFP::elmd-1 (C56G7.3)::unc-54 3'UTR +rol-6}* (OIK1045) were crossed into *wdr-31(T05A8.5)(tm10423)II., elmd-1(syb630) II,* double and *wdr-31(T05A8.5)(tm10423)II., elmd-1(syb630) II, rpi-2(K08D12.2)(ok1863) IV.* triple mutants. *N2;turEx21[arl-13p::wdr-31 (T05A8.5)::GFP::unc-54 3'UTR +rol-6} (1 ng)* (OIK1042) were mated with *T05A8.5(syb1568)II., elmd-1(syb630) II, rpi-2(K08D12.2)(ok1863) IV.* triple mutants. Plasmid (*arl-13p::wdr-31 (T05A8.5)::GFP::unc-54 3'UTR*) was directly microinjected into triple mutant *T05A8.5(syb1568)II., elmd-1(syb630) II, rpi-2(K08D12.2)(ok1863) IV* (1 ng). *dpy-5(e907);nxEx386[rpi-2::gfp + dpy-5(+)]* (MX352) were crossed into *wdr-31(T05A8.5)(tm10423)II., elmd-1(syb630) II, rpi-2(K08D12.2)(ok1863) IV.* triple mutants. Three independent Dye uptake assays were performed, and fluorescence filters were set for GFP and Texas Red, followed by fluorescence imaging (20-150 heads and tails were counted). Dye uptake of mutants with corresponding transgenics strains was compared to that of non-transgenic strains in the same rescue plates **(Fig. S2C, D)**.

Generation of mutants using CRISPR/Cas9 in the nematode *Caenorhabditis elegans*

To generate *wdr-31(T05A8.5)(tur003)* allele, three sgRNAs targeting *C. elegans* T05A8.5 (human WDR-31) were chosen using an online tool, Benchling [Biology Software] (2019), followed by ordering complementary oligonucleotides (Macrogen, South Korea), and cloning of sgRNAs into an empty sgRNA vector pRB1017. The successful sgRNA insert was confirmed with colony PCR,

161 followed by plasmid isolation. Three sgRNAs (each 50 ng/µl) were injected into the gonads of
162 wild type together with pDD162 (*Peft-3::Cas9;* 15 ng/ µl plasmid pRF4) and pRF4 (50 ng/ µl
163 plasmid pRF4) (Dickinson et al., 2013). F1s with the roller phenotype were identified, and after
164 they generated enough progenies, the PCR technique was used to identify the F1 generation
165 bearing the predicted deletion, as well as the homozygosity of the allele mutation. The PCR
166 products from knockout animals were then sent to the Sanger sequencing (Macrogen, South
167 Korea). *wdr-31(*tur003*)II.* mutants have 1276-bp deletion covering a huge part of exon II (297 bp
168 out of 359 bp) and whole exon III, IV, and exon V. This is likely a null allele of *wdr-31.* sgRNA
169 sequences can be found in Table S1.
170
171 **Generation of transgenic strains and strain list for *C. elegans***
172 To generate transgenic lines for localization, rescue experiments, and expression patterns, we
173 generated the following transgenic animals via microinjections.
174 *OIK1042 turEx21[arl-13p::wdr-31 (T05A8.5)::GFP::unc-54 3'UTR +rol-6}*;
175 *T05A8.5(syb1568)II., elmd-1(syb630) II, rpi-2(K08D12.2)(ok1863) IV.* (1 ng)
176 *OIK1044 N2;turEx23[elmd-1p::GFP::elmd-1 (C56G7.3)::unc-54 3'UTR +rol-6}* (5 ng)
177 *OIK1045 N2;turEx24[arl-13p::GFP::elmd-1 (C56G7.3)::unc-54 3'UTR +rol-6}* (5 ng)
178 *OIK1046 N2;turEx25[elmd-1p(C56G7.3)::GFP::unc-54 3'UTR +rol-6}* (50 ng)
179 *OIK1047 N2;turEx26[wdr-31 (T05A8.5)p::GFP::unc-54 3'UTR +rol-6}* (50 ng)
180 The rol-6 plasmid (50 ng/ µl plasmid pRF4) was co-injected as the co-transformation marker. In
181 brief, the plasmids were delivered by microinjections into the gonads of 1-day adult worms.
182 Worms were initially transferred onto a 2.5% agarose pad prior (Halocarbon oil, Sigma: 9002-83-
183 9), followed by microinjection. The microinjection was done using a Zeiss Axio Vert.A1 inverted

184 microscope with DIC optics coupled with a Narishige Micromanipulator MMO-4. We next
185 manually inspected the plates to find successful transgenics animals.
186 **Wild Type and mutant alleles:** N2; *FX30333; wdr-31*(*T05A8.5)(tm10423)II.; OIK393*
187 *T05A8.5(tur003)II.; PHX1568 T05A8.5(syb1568)II.; nphp-4(tm925)V.; mks-6(gk674)I.;*
188 *PHX630, elmd-1(syb630) III.; RB1550 rpi-2(K08D12.2)(ok1863) IV.*; *MX52, bbs-8(nx77) V.* We
189 obtained *wdr-31(T05A8.5)(tm10423)II. (FX30333)* mutant allele, which has a 160-bp deletion,
190 causing a frameshift, from the National Bioresource Project, Japan. The *wdr-*
191 *31(T05A8.5)(tm10423)II.* were outcrossed to wild type four times. The Caenorhabditis Genetics
192 Center (CGC), Minnesota, USA, provided the *RB1550 rpi-2(K08D12.2)(ok1863)* mutant, and the
193 *rpi-2(ok1863)* allele contains 1143-bp deletion that removes a large segment of exon III, exon IV,
194 and some portion of exon V. *T05A8.5(syb1568)II.* has 1888-bp deletion, deleting all exons except
195 exon I **(Supplementary Fig. 3B)**. Sunybiotech created an independent null allele of *elmd-1* via
196 CRISPR–Cas9. The *PHX630, elmd-1(syb630) III.* mutant contains 1784-bp deletion, where except
197 for exon I, all exons were removed **(Supplementary Fig. 2B)**. *elmd-1(syb630) III.* were outcrossed
198 to wild type two times.
199
200 **Fluorescent transgenes for IFT proteins:** *GOU2162 che-3(cas443[gfp::che-3]) I; xbx-*
201 *1(cas502[xbx-1::tagRFP]) V ; GOU2362 ift-74(cas499[ift-74::gfp]) II.; EJP76 vuaSi15*
202 *[pBP36; Posm-6::osm-6::eGFP; cb-unc119(+)] I; unc-119(ed3) III; osm-6(p811) V;*
203 *N2;lqIs2[osm-6::gfp], N2;ejEx[osm-3::GFP + pRF4]; N2;ejEx[kap-1::gfp+pRF4]; EJP81*
204 *vuaSi24 [pBP43; Pift-140::ift-140::mCherry; cb-unc-119(+)]II; unc-119(ed3) III; ift-*
205 *140(tm3433) V; jhuEx [ift-140::GFP+pRF4]; Ex[rpi-2::GFP+ xbx-1::tdTomato+pRF4]; MX76*
206 *dpy-5(e907); nxEx(bbs-7::gfp+dpy-5 (+)).*

Fluorescent transgenes for ciliary proteins: PHX1180, *wdr-31(syb1180 [wdr-31(T05A8.5)::GFP]); PHX4934 rpi-2(syb4934) [rpi-2::mCherry]; OIK1042 N2;turEx21[arl-13p::wdr-31 (T05A8.5)::GFP::unc-54 3'UTR +rol-6} (5 ng); OIK1044 N2;turEx23[elmd-1p::GFP::elmd-1 (C56G7.3)::unc-54 3'UTR +rol-6} (5 ng); OIK1045 N2;turEx24[arl-13p::GFP::elmd-1 (C56G7.3)::unc-54 3'UTR +rol-6} (5 ng); OIK1046 N2;turEx25[elmd-1p(C56G7.3)::GFP::unc-54 3'UTR +rol-6} (50 ng); OIK1047 N2;turEx26[wdr-31 (T05A8.5)p::GFP::unc-54 3'UTR +rol-6} (50 ng)*; *N2;Ex[mks-2::GFP + tram-1::tdTOMATO + pRF4]; MX1409 N2; nxEx785[tax-4:gfp+ Posm-5::xbx-1::tdTomato + rol-6(su1006)]; vuaSi21[pBP39; Pmks-6::mks-6::mCherry; cb-unc-119(+)]II; MX2418 N2;nxEx1259[pbbs-8::PLC-delta PH::GFP;MKSR-2::tdTomato; coel::GFP]; PY8847 oyIs65[str-1p::mcherry]; Ex[str-1p::nphp-4::gfp, unc122p::dsRed]*. All PHX strains were generated using CRISPR/Cas9 by Sunybiotech. The list of extensive transgenic and mutant strains was provided in Table S2.

Fluorescence and Confocal microscopy for *C. elegans*

Fluorescence images (dye assay) and time-lapse movies (IFT movies) were captured using an epi-fluorescence upright microscope (Leica DM6 B) (3 frames per second, and up to 120 frames). The epi-fluorescence upright microscope was controlled with iQ3.6.2 Andor software and was attached with an Andor iXon Ultra 897 EMCCD (an electron-multiplying charge-coupled device camera). The LSM900 confocal microscope with Airyscan 2 (ZEN 3 Blue edition software) was used to capture the high-resolution Z-stack images. On microscope slides, a drop of 2-3% agarose was used to create an agarose pad, and worms were then moved to the agarose pad containing 1-3 µl of 10 mM levamisole (an anesthetic agent). Images were collected at 0.14 m intervals with a Plan

ApoChromat 63x/1.40 NA target, then analyzed with Blue edition software ZEN 3 to create Z-stacks, and processed with ImageJ (NIH) software (Schneider et al., 2012).

In vivo intraflagellar transport assay for IFT frequency and velocity

The time-lapse movies of GFP-labelled IFT proteins were analyzed with the automatic kymograph analyzing tools KymographClear and KymographDirect, both of which are ImageJ based (Mangeol et al., 2016; Turan et al., 2022). KymographClear was used to produce kymographs from time-lapse movies. We examined each produced kymograph and calculated IFT frequency or IFT velocities for IFT-74::GFP (an endogenously tagged), GFP::CHE-3 (an endogenously tagged), BBS-7::GFP (an overexpression transgene), OSM-6::GFP (a single copy transgene), OSM-3::GFP (an overexpression transgene), and IFT-140::GFP (an overexpression transgen) in wild type, *wdr-31;elmd-1* double and *wdr-31;elmd-1;rpi-2* triple mutants. All worms were maintained at 20 °C for IFT analysis. At least ten IFT videos were taken over three separate time periods for strains, and IFT particles from at least ten kymographs were counted.

Whole-mount *in situ* hybridization in zebrafish

Whole-mount in situ hybridization was performed as previously described (Thisse et al., 2004). The *wdr31* cDNA with T7 promoter was PCR amplified, with forward primer: ATGGGGAAGCTACAGAGCAAGTTC and reverse primer: TAATACGACTCACTATAGAAGCGAGCCACTTCAGTGATACTG, from a homemade cDNA library of zebrafish embryos at 24 hpf. The antisense probe for *wdr31* was then transcribed with digoxigenin-labeled UTPs and T7 RNA polymerases (Roche, Basel, Switzerland). The stained embryos were dehydrated in glycerol and photographed with a Nikon SMZ1500 stereomicroscope (Nikon, Tokyo, Japan).

Mutagenesis of *wdr31* in zebrafish using the CRISPR/Cas9 technology

Generation of zebrafish mutants using the CRISPR/Cas9 system was carried out as previously described (Chang et al., 2013). Briefly, two gRNAs targeting sequences in *wdr31* were chosen as following: 5'- ACCCATGTGTGTTGGGTACC-3' and 5'-GAAGCCATCCAGGAGTTCAG-3'. gRNA templates were PCR amplified and gRNAs were *in vitro* transcribed with T7 transcriptase (NEB, cat# M0251S). gRNAs and Cas9 protein (NEB, cat# M0251S) were simultaneously injected into the embryos at one-cell stage.

Immunofluorescence staining and microscopy

Immunostaining was performed as previously described (Xu et al., 2017). Briefly, embryos were fixed in cold Dent's fixative (80% methanol: 20% dimethyl sulfoxide) at -20°C overnight and then stored in methanol. Samples were permeabilized with 0.005% (m/v) trypsin for 30 minutes. Samples were blocked with blocking buffer (10% [v/v] goat serum in PBST), followed by incubation with primary antibody anti–acetylated tubulin (1:2000; Sigma-Aldrich, St. Louis, MO) and then secondary antibodies conjugated with Alexa Fluor 568 (1:500; Invitrogen, Carlsbad, CA). Samples were mounted on ProLong Gold Antifade Mountant with DAPI (Invitrogen) and images were taken with a Nikon A1R confocal microscope.

Software and algorithms

Zen Blue	Zeiss	https://www.zeiss.com/corporate/int/home.html
Andor iQ3	Andor	https://andor.oxinst.com/
Fiji	ImageJ	https://fiji.sc
ImageJ	ImageJ	https://imagej.nih.gov/ij/
Illustrator (CS5.1)	Adobe, USA	https://www.adobe.com/
KymographClear	Peterman Lab	https://sites.google.com/site/kymographanalysis

277 R R Core Team https://www.r-project.org/

278

279 **Statistical analysis and Generating Figures**

280 For statistical analysis of dye assay, Fisher's exact test (one tailed tests) was performed. For data
281 involving continuous variables like IFT speed and cilia length, Mann-Whitney U-test or Welch's
282 t-test was used depending on the distribution of data. Transgenic worms were kept at 15 °C for
283 AWB cilia morphology analysis and AWB cilia length measurements, and only L4 stage animals
284 were imaged for AWB cilia. For each strain, at least three independent microcopy analyses were
285 performed, and 60-220 AWB cilia were examined. All statistical tests were performed using R
286 software. The codes and files needed to generate figures and perform statistical analysis were
287 openly shared, and the files and codes for making figures and performing statistical analysis may
288 be accessed at https://github.com/thekaplanlab/WDR31-ELMOD-RP2.

289 **Gateway Cloning (mammalian constructs)**

290 Constructs for ELMOD3 (HsCD00288286) and WDR31 (HsCD00045652) were purchased
291 from Harvard Medical School. LR Reaction (Invitrogen, USA) was performed to transfer the target
292 sequence into destination vectors ((N)RFP, (N)CFP plasmids) with a subsequent transformation
293 into *E. coli* DH5α. DNA was isolated according to Monarch® Plasmid Miniprep Kit (BioLabs,
294 USA) and the PureYield® Plasmid Midiprep Protocol System (Promega, USA). Verification of
295 successful cloning was done by sequencing (Eurofins, Luxembourg).

296

297 **Immunofluorescence Staining (Mammals)**

298 hTERT-RPE1 cells were transiently transfected according to Lipofectamine™ 3000 Reagent
299 Protocol with ELMOD3-CFP and WDR31-RFP constructs followed by serum starvation for three

300 days to induce cilia formation. Cells were fixed with 4% PFA for 45min at 4°C, permeabilized for
301 5min with 0.3% PBST and blocked with 10% goat serum in PBST at 4°C overnight. A primary
302 antibody for ARL13B (1:50; Proteintech, Germany) and a secondary antibody conjugated to Alexa
303 Fluor 647 (1:350; Invitrogen, USA) were used. Cells were mounted using Fluoromount-G
304 (Invitrogen, USA).

305 **Microscopy Setup (Mammals)**

306 Images were captured using a Leica TCS SP8 scanning microscope (Leica Microsystems IR
307 GmbH, Germany). The setup includes 488 nm, 532 nm and 635 nm pulsed excitation lasers as
308 well as 100x oil immersion objective lens (NA 1.4) and a hybrid detector (HyD). Pixel number
309 was 1024 x 1024 and optimal pixel size was determined by Nyquist calculation resulting in a size
310 of 43 × 43 nm in XY. Additionally, Z-steps should not exceed 131 nm when acquiring a stack.
311 Laser intensity was adjusted for each sample and images were recorded with 2x frame averaging.

312 **Image Processing (Mammals)**

313 Acquired images were processed (LasX, Leica Microsystems), deconvoluted (Huygens Software,
314 SVI, Netherlands) and edited (FIJI software). The deconvolution was performed with a Classical
315 Maximum Likelihood Estimation (CMLE) algorithm under experimentally defined settings. The
316 background level was software estimated, the quality threshold was 0.001, the number of iterations
317 was 50 and signal-to-noise ratio was set to 20. All images were brightness-corrected for the
318 purpose of presentation.

319

320 **Results**

321 **WDR31 and ELMOD are evolutionarily conserved constituents of cilia**

As part of our ongoing effort to reveal novel cilia genes, using single-cell RNA-seq data, we conducted comparative expression analysis in *C. elegans* and discovered that the WDR31 and ELMOD orthologues, WDR-31 (T05A8.5) and ELMD-1 (C56G7.3), are likely expressed exclusively in ciliated sensory neurons (manuscript in preparation). The head (amphid) and tails (phasmid) of *C. elegans* contain a total of 60 ciliated sensory neurons, and the expression patterns of genes can be reliably analyzed using fluorescence tagged promoter markers. Consistent with our predictions, promoter-based GFP reporters revealed that both WDR-31 and ELMD-1 are expressed in most of the ciliated sensory neurons **(Fig. S1A)**. To explore if both proteins are concentrated within cilia, we investigated their subcellular localization in *C. elegans* and created CRISPR/Cas9-mediated knock-in of WDR-31::GFP and a transgenic animal expressing GFP-tagged ELMD-1. The endogenously expressed WDR-31::GFP is concentrated at the ciliary base in both head and tails, where it colocalizes with the basal body marker γ-tubulin (TBG-1, the ortholog of human TUBG1), and the IFT-140 (human IFT140) basal body signal **(Fig. 1A, B, C, and D)**, so our co-localization data suggests that WDR-31 is a new cilia-associated protein. ELMD-1 is the sole orthologue of the three human ELMOD proteins (ELMOD1-3) that function as GTPase-activating proteins (GAP). We found that GFP::ELMD-1 localizes to the periciliary membrane compartment (PCMC) and the basal body (BB) (marked with IFT-140), but is proximal to the MKS-6-labeled transition zone that is adjacent to the BB **(Fig. 1E, F, and G)** (Kaplan et al., 2012).

To determine if both human WDR31 and ELMOD3 (also known RBED1, the top blastp hit for *elmd-1*) are concentrated within cilia in mammalian cell lines, we generated hTERT-RPE1 cells co-expressing WDR31-RFP and ELMOD3-CFP and stained them with a ciliary marker ARL13B. Furthermore, WDR31-RFP or ELMOD3-CFP were transiently transfected into hTERT-RPE1

cells, and they were additionally stained for ARL13B. Our super-resolution microscopy analysis revealed that both WDR31 and ELMOD3 are enriched in the cilium **(Fig. 2A, B and Fig. S2B and C)**. Taken together, our complementary approach demonstrates that both WDR31 and ELMOD3 are evolutionarily conserved proteins associated with cilia.

Wdr31 regulates ciliogenesis in the Zebrafish ear

We turned our interest into zebrafish to develop an *in vivo* model for WDR31 to examine the role of WDR31. We first used the whole-mount *in situ* hybridization (ISH) within zebrafish to visualize the expression pattern of *wdr31* during zebrafish embryo development up to 1-day post-fertilization. The dynamic and wide expression of *wdr31* during zebrafish embryonic development (2 cell and 8 somite stages (SS)) has become restricted to the otic vesicle and brain region at 24 hours post-fertilization (24 hpf) **(Fig. 3A)**. We next knocked out (KO) *wdr31* in zebrafish with the CRISPR/Cas9 system and the embryos showed heart edema and otolith malformation. As *wdr31* is expressed in the otic vesicle and the otolith development requires cilia, we checked the cilia in the otic vesicle. The cilia bundle in the lateral crista (LC) of the otic vesicle was stained with acetylated tubulin in wild type and *wdr31* KO, and although we found that the length of LC cilia was comparable with wild type, the width of the cilia bundle was reduced by 33% in LC of the otic vesicle compared to that in the control embryos, suggesting the cilia number is decreased **(Fig. 3B, C, and D).** Our zebrafish work indicates that WDR31 plays a role in ciliogenesis in the zebrafish ear.

Functional redundancy of WDR31, ELMOD, and RP2 for determining cilia morphology

We next wanted to gain mechanistic insight into the functions of *wdr-31* in cilia biogenesis. To this end, we employed the nematode *C. elegans* and obtained/generated three *wdr-31* alleles:

tm10423 (160-bp frameshift causing deletion), syb1568 (1888-bp deletion removing all exons except exon I), and tur003 (1276-bp deletion removing a large portion of exon II and exon III, IV, and exon V) (**Fig. S3B)**. In *C. elegans,* the lipophilic fluorescent dye-uptake assay is employed to indirectly evaluate the cilia structure, and our analysis revealed *wdr-31* mutants display wild type level dye-uptake in both head (amphid) and tail (phasmid), suggesting cilia structures are likely unaffected in these mutants **(Fig. 4B and Fig. S4A)**. To address whether loss of *wdr-31* leads to subtle defects in cilia morphology, we expressed the fluorescence-based marker *str-1pro:mCherry, gcy-5pro::gfp, srb-6pro::gfp ,* which label the AWB, ASER and PHA/PHB cilia, respectively, in *wdr-31* mutants. The AWB dendritic tip extends the fork-like cilia in the wild type, and rod-like cilia protrude from the dendritic endings of ASER and PHA/PHB sensory neurons. Our confocal microscopy analysis revealed that the structure and length of ASER, PHA/PHB, and AWB cilia are comparable with those of wild type cilia, suggesting, contrary to the importance of WDR31 for ciliogenesis in the zebrafish ear, the loss of *wdr-31* alone does not result in a severe defect in cilia structure **(Fig. 4C, D, E, F, and G)**.

The lack of an apparent cilia phenotype in *C. elegans* may be attributed to a functional redundancy for WDR-31 in cilia biogenesis, and functional redundancy is indeed a common phenomenon in ciliopathy-related genes. For example, while the absence of individual ciliopathy genes encoding MKS/MKSR proteins or NPHP proteins (NPHP-1, NPHP-4) does not result in serious cilia defect, the loss of *nphp-4* (the ortholog of human NPHP4) in combination with *mks-6* (the ortholog of human CC2D2A) causes more severe cilia related defects (transition zone membrane association defects) (Williams et al., 2011). We next explored genetic interaction between *wdr-31* and *elmd-1*, since our results showed that both protein products are at the ciliary base **(Fig. 1C, D, E, and F)**. We discovered that the *wdr-31(tm10423);elmd-1(syb603)* double

mutant (hereinafter referred to as "double mutant") has a partial Dyf defect in both head and tail neurons, which was rescued by expression of a transgene containing the wild type *elmd-1* sequence **(Fig. 5B and Fig. S4A,** $p < 0.0001$, Fisher's exact test**)**. Using the AWB, ASER and PHA/PHB cilia fluorescence markers, we subsequently set out to visualize the ciliary structures in the double mutant and single mutants. The AWB cilia in the double mutants have an extra projection in the middle part of the cilia (7% (N: 100) and 52 % (N: 134) in WT and double mutant, respectively), whereas ASER, AWB, and PHA/PHB cilia are normal length in WT and double mutant **(Fig. 4C and D, E, and F and Fig. S4B)**.

We explored genetic interaction between *wdr-31, elmd-1,* and *rpi-2* (the X-linked retinitis pigmentosa protein RP2 and a GTPase-activating protein) since ELMD-1 and WDR-31 localizations are reminiscent of RPI-2 localization (the endogenously labeled RPI-2) in *C. elegans* (**Fig. 4A, and Fig. S5A)** (Williams et al., 2011). We, therefore, first generated an *elmd-1;rpi-2* double mutant, which revealed no Dyf phenotype **(Fig. 4B, and Fig. S4A)**. However, when we created *wdr-31;elmd-1;rpi-2* triple mutants (hereinafter referred to as "triple mutant"), we observed severe synthetic Dyf phenotype, which is significantly rescued by the introduction of a wild-type copy of *wdr-31* or *elmd-1 or rpi-2* **(Fig. 4B, Fig. S3C, and Fig. S4A** $p < 0.0001$, Fisher's exact test**)**.

We then sought to examine AWB, ASER and PHA/PHB cilia morphology in triple mutants and compared them with the *wdr-31;elmd-1* and *rpi-2;elmd-1* double mutants. The Dyf defect of triple mutants was indeed accompanied by significant changes in these cilia. The AWB cilia displayed the ectopic projections, including a backward projection from the base of AWB cilia in triple mutant and as wells as ectopic projections from the middle part of AWB cilia (0% backward projection in wild type vs over 30% backward projection in triple mutant; $p < 0.0001$, Fisher's

exact test) (**Fig. 4F and G**). It is noteworthy that the similar backward projections in AWB cilia were observed in two independent triple mutants generated with *wdr-31(syb1568)* and *wdr-31(tur003)* (**Fig. S7A and B**). A backward projection from the ciliary base was observed for ASER cilia, but not PHA/PHB cilia in triple mutants (**Fig. 4F)**. We next measured the cilia lengths of these cilia and discovered that ASER and PHA/PHB cilia are significantly shorter in triple mutants (20% shorter for ASER in triple mutants, 13% shorter for PHA/PHB in triple mutants), whereas the cilia length of AWB cilia was not significantly altered in triple mutants **(Fig. 4C, D, F, and Fig. S4B)**. This establishes a role for WDR-31 in controlling cilia length and morphology in a subset of sensory neurons in a redundant manner with RPI-2 and ELMD-1.

WDR-31-ELMD-1-RPI-2 are needed for effective cilia entry and exit of IFT components.

We next aimed to investigate the mechanism by which WDR-31, ELMD-1, and RPI-2 regulate cilia morphology in *C. elegans.* To this end, we investigated whether these genes affect the localization of IFT proteins and IFT motors, including kinesin motors (Kinesin II and OSM-3/KIF17), dyneins, and IFT components (IFT-A and IFT-B). The IFT complex and motor proteins are critical for cilia construction and maintenance because they deliver ciliary constituents from the cell body to the cilia. In *C. elegans,* two kinesin motors Kinesin II and OSM-3/KIF17 (heterotrimeric kinesin-II and homodimeric OSM-3) work cooperatively to carry the IFT complex in the middle segment of the channel cilia in an anterograde direction, while OSM-3/KIF17 transports the entire IFT complex (IFT-A, IFT-B, and BBSome) in the distal part of channel cilia.

We generated single, double, and triple mutants expressing fluorescence tagged IFT and motor proteins. Using single-copy transgenes, we found that IFT-B components predominantly accumulate at cilia tips and/or middle of cilia in double mutants (96% ciliary tip accumulations for IFT-74/IFT74, N: 26 and 82% ciliary tip accumulations for OSM-6/IFT52, N: 46) but the

localization of GFP::CHE-3 (human dynein heavy chain DYNC2H1) remains less affected in double mutants (27% minor middle cilia accumulations for CHE-3; N: 48, see supplementary Movie S1) **(Fig. 5A, C and D and Supplementary Movie S1, 2, 4)**. Furthermore, we next investigated the localization of GFP::CHE-3 in triple mutants because the cilia morphology of triple mutants is more severe than that of *wdr-31;elmd-1* or *wdr-31;rpi-2* or *elmd-1;rpi-2* double mutants (**Fig. 5A).** Compared with wild type and double mutants, we noticed additional IFT abnormalities in two independent triple mutants, including dim cilia staining with GFP::CHE-3 and accumulations of GFP::CHE-3 in the middle/distal part of cilia (81% middle cilia accumulations, N: 96; 6.6% ciliary tip accumulations, N: 90) (**Fig. 5A and Supplementary Movie S1)**. Motor protein OSM-3/KIF17 accumulation within the ciliary tips was detected in double and triple mutants **(Fig. 5B, and Supplementary Movie S3)**. Furthermore, in triple mutants, the dim distal cilia staining was observed for IFT-140::GFP (IFT-A component) (63% dim distal cilia, N: 47) and XBX-1::mCherry (a dynein light intermediate chain) **(Fig. 5E and F and Supplementary Movie S5)**, but the ciliary distribution of KAP-1::GFP (Kinesin II) remains unaffected **(Fig. 5G)**.

Cilia accumulations of IFT-B components and OSM-3/KIF17 coupled with weak cilia staining with IFT-A components in triple mutants forced us to better understand the role of WDR-31-ELMD-1-RPI-2 in IFT defects, we therefore employed *in vivo* time-lapse video coupled with kymography. For a subset of IFT components, we detected a significant decline in the quantity of IFT particles traveling along the cilia in both directions in double and triple mutants (**Figure 6A, B, C, D, E, E, G, and H**). We found significant decline in the IFT transport for kinesin motor OSM-3::GFP in double and triple mutants in both anterograde and retrograde directions (the anterograde and retrograde: 0.68 n/s and 0.61 n/s in wild type; 0.43 n/s and 0.32 n/s in double mutants; 0.34 n/s and 0.23 n/s in triple mutants, $p < 0.0001$; the Mann–Whitney U test) (**Fig. 6A,**

464 **and B**), while our analysis revealed that the flux of cytoplasmic dynein motor protein CHE-3 along
465 the cilium was unchanged in both directions in both double and triple mutants (**data not shown**),
466 suggesting, indicating that the simultaneous elimination of these genes has an effect on the kinesin
467 motor OSM-3 but not on cytoplasmic dynein loading onto IFT, but their absence leads to both
468 ciliary cytoplasmic dynein accumulation and the kinesin motor OSM-3 (**Fig. 5A and B**). In wild
469 type, the average of IFT-74 particles moving in anterograde and retrograde directions is 0.58 (n/s:
470 number of particles/seconds) and 0.52 n/s, respectively, while in triple mutants, the anterograde
471 and retrograde IFT-74 particles are 0.27 n/s and 0.09 n/s. Comparable reductions were observed
472 for IFT-74::GFP (CRISPR tagged endogenous IFT-74) in *wdr-31;eldm-1* double mutant (0.36 n/s
473 and 0.21 n/s in *wdr-31;eldm-1;* $p < 0.0001$; the Mann–Whitney U test) (**Fig. 6G, and H**). For
474 OSM-6::GFP, the anterograde and retrograde IFT particles statistically differ between wild type
475 and triple mutants (the anterograde and retrograde: 0.52 n/s and 0.58 n/s in wild type, 0.36 and
476 0.30 in triple mutants*;* $p < 0.0001$; the Mann–Whitney U test) (**Fig. 6E, and F**). Furthermore, IFT-
477 A component IFT-140 transport declined in both directions both double and triple mutants (**Fig.**
478 **6C, and D**). Taken together, our fluorescent microscopy analysis reveals several IFT abnormalities
479 in triple mutants: first, in triple mutants, there is a significant decrease in the quantity of IFT
480 particles, including the OSM-3/KIF17 kinesin motor and both IFT-A and IFT-B components,
481 traveling in both anterograde and retrograde directions. Second, the ciliary accumulations of IFT-
482 B components and OSM-3/KIF17 kinesin motors in cilia together with weak distal cilia staining
483 of the IFT-A component and dynein (XBX-1) in triple mutants suggest that the defects in the return
484 of IFT from the ciliary tips. These defects might stem from a reduction in the loading of IFT
485 components and dynein onto IFT trains at the ciliary base.
486
487

To better investigate the role of WDR-31, ELMD-1, and RPI-2 in IFT, we measured the anterograde (middle and distal segment) and retrograde IFT velocities in wild type and triple mutants. When compared to wild-type IFT speeds, we found a significant increase in the average anterograde IFT velocities of IFT-74::GFP, IFT-140::GFP, OSM-3::GFP, and OSM-6::GFP in the middle segments of triple mutant (**Fig. S7A, B, C, and D**), implying that the integrity of anterograde IFT components is likely compromised. In contrast, in the triple mutant, the retrograde and distal anterograde IFT velocities are unaltered. Taken together, our findings suggest that with the exception of heterotrimeric Kinesin II, all IFT proteins studied, including dynein CHE-3, OSM-3 kinesin, IFT-B, and IFT-A components, display certain defects in *wdr-31* related mutants, either ciliary accumulations for dynein CHE-3, OSM-3 and IFT-B component or dim distal cilia staining for IFT-A component and dynein motors (CHE-3 and XBX-1) or changes in IFT velocities.

WDR-31, ELMD-1, and RPI-2 restrict ciliary entry of non-ciliary proteins

Given that WDR-31, ELMD-1, and RPI-2 localize at the base of cilia, we wanted to examine the role of these proteins in the ciliary gate, and we chose the TRAM-1 protein (the ortholog of human TRAM1), which surrounds the PCMC in *C. elegans* but stays outside of cilia (Williams et al., 2011), as well as the transition fiber protein DYF-19 (human FBF1) and the transition zone proteins NPHP-1 (the human NPHP1) and MKS-2 (human TMEM216) (Wei et al., 2013). We showed that neither *wdr-31, elmd-1*, or *rpi-2* deletion, nor double mutant combinations, result in ciliary entry of TRAM-1 or MKS-2 (**Fig. 7A and B)**, suggesting that neither of these alone affects ciliary gating. In contrast, TRAM-1 protein leaks into cilia in all three independent *wdr-31* triple mutants, but the majority of signal remains outside of cilia (**Fig. 7A and B**), whereas the

localizations of transition zone NPHP-1 and transition fiber protein DYF-19 remain unchanged (**Fig. 7C**). In the *wdr-31;elmd-1;rpi-2* triple mutants, the PLC1-PH::GFP marker for phosphatidylinositol 4,5-bisphosphate (PtdIns(4,5)P2) stays outside of cilia. In the wild type, PLC1-PH::GFP stains PCMC membranes but does not penetrate cilia (**Fig. 7D)**. Furthermore, we explored the localization of TAX-4, a ciliary membrane protein, and it remains unaffected in the triple mutants (**Fig. 6SB**). Taken together, our findings reveal a functionally redundant role for WDR31, ELMD-1, and RPI-2 in restricting entry of non-ciliary proteins into cilia, despite the fact that TZ protein localization remains unchanged.

WDR-31 and ELMD-1 are required for recruitment of BBS-7, a BBSome component, to cilia

Some of IFT defects (cilia accumulations of IFT-B complex, weak cilia staining of IFT-A components, and increased in IFT speed) observed in the *wdr-31;elmd-1;rpi-2* triple mutants are reminiscent of IFT defects observed in several *bbs* mutants (Blacque, 2004; Ou et al., 2005; Wei et al., 2012; Xu et al., 2015;). We hypothesized that the IFT complex destabilization defects in triple mutants might be due to defects in the BBSome. First, we found that ciliary tip accumulations of IFT-74:GFP, an IFT-B component, in *bbs-8(nx77)* mutants were comparably similar to that of double and triple mutants (**Fig. 9A**). Furthermore, there is no further increase of IFT accumulations in the triple mutants *wdr-31;elmd-1;bbs-8*.

We then investigated whether the ciliary localization of BBS-7::GFP, a core member of the BBSome, is controlled by WDR-31, ELMD-1, and RPI-2, because the ciliary localization of other BBSome components is dependent on other BBSome subunits (Ou et al., 2007). We predict that the ciliary localization of BBSome is more likely disturbed in triple mutants, contributing to

the observed IFT abnormalities. Consistent with expectations, BBS-7::GFP is lost or significantly diminished in the cilia of double and triple mutants, but BBS-7::GFP localization persists at the ciliary base in these mutants (**Fig. 9B**). We next performed the time-lapse movie analysis of BBS-7::GFP with kymography, which revealed that BBS-7::GFP movements were undetectable in 27% and 42% of cilia in the head in double and triple mutants, respectively (**Supplementary Movie S6)**. We were able to quantify the frequency of BBS-7::GFP even though the density of trajectories (IFT particles) on kymographs was weak in double and triple mutants relative to wild type (**Fig. 9C**). Our analysis revealed a substantial decrease in the average of BBS-7::GFP particles translocating in the anterograde and retrograde directions in the remaining worms that display IFT (average anterograde and retrograde IFT particles: 0.55 n/s and 0.58 for wild type; 0.30 n/s and 0.33 n/s for double mutant; 0.07 n/s and 0.07 n/s for triple mutant, $p < 0.0001$; the Mann–Whitney U test) (**Fig. 9C, D and Supplementary Movie S6**). We next used IFT-74::GFP to investigate IFT speeds in *bbs-8* and its mutant combinations with *wdr-31* and *elmd-1*. The average velocities of IFT-74::GFP in the middle segment of *bbs-8;wdr-31* and *bbs-8;wdr-31;elmd-1* were higher than wild type, but were comparable to the *wdr-31;elmd-1;rpi-2* triple mutant (**Fig. S7A**). Taken together, our results suggest that because the BBSome complex is unable to gain access to cilia in double and triple mutants, IFT-B components and OSM-3/KIF17 likely accumulate excessively in the distal portion of the cilia while IFT Complex A component staining the distal segment cilia become dim (**Fig. 9E**).

Discussion

WDR31 is a new ciliary protein encoding gene required for cilia biogenesis

Clinical genomics, proteomics, functional genomics, and bioinformatics research have all contributed to the expansion of the list of both ciliary and ciliopathy genes. Over 300 genes have been identified as encoding ciliary proteins, including IFT-kinesin-dynein components, BSSome components, structural ciliary components, signaling molecules, and IFT regulators, with many of them being ciliopathy genes (Wheway et al., 2019; Vasquez et al., 2021). Our findings reveal the roles of WDR-31, a member of the WD40-repeat protein (WDR) family, the ELMOD orthologue (ELMD-1) and RP2 orthologue (retinitis pigmentosa 2; RPI-2) in cilia and IFT regulation. Several members of the WD40-repeat protein family, including WDR34, WDR35, and WDR60, have previously been connected to cilia, but the role of *WDR-31* in cilia has been unknown (Blacque et al., 2006; Patel-King et al., 2013; Rompolas et al., 2007). Strikingly, we found that WDR31 is a ciliary protein, and knocking it out in zebrafish using CRISPR/Cas9 causes ciliary defects, including a decrease in the number of cilia in the LC. Furthermore, the link between WDR31 and cilia was significantly strengthened by findings from *C. elegans*. First, the expression of the *WDR31* orthologue (WDR-31) is restricted to the ciliated sensory neurons, and WDR-31 is localized to ciliary compartments (the ciliary base and cilia) in C. elegans and human TERT-RPE1 cells. The exclusive cilia expression pattern of *wdr-31* in *C. elegans* is similar to that of ciliary and ciliopathy genes like ARL-13/ALR13B, IFT, and BBS (Blacque et al., 2005). Second, CRISPR/Cas9 mediated knock out of *WDR-31* combination with the ELMOD orthologue (ELMD-1) and RP2 orthologue (retinitis pigmentosa 2; RPI-2) results in an abnormality in cilia functions and structure in *C. elegans*. Our findings reveal that WDR31 is a new ciliary protein required for cilia morphology in both zebrafish and *C. elegans*, suggesting the evolutionarily conserved role of WDR31 in cilia biology.

Functional redundancy between WDR-31, ELMD-1, and RPI-2

Our genetic analysis in *C. elegans* provides evidence for functional redundancy for *wdr-31*, *elmd-1*, and *rpi-2* in regulating cilia length, cilia morphology, and the trafficking of kinesin-IFT-BBSome complexes. Though cilia length and cilia morphology are disrupted in *wdr-31;elmd-1;rpi-2* triple mutants, with altered recruitment of kinesin, IFT, and BBS proteins and IFT dynamics, simultaneous elimination of *elmd-1* and *rpi-2* did not result in severe defects in cilia and IFT. Our interpretation for these data is that the additive defects in the triple mutants were likely due to *wdr-31*, and WDR-31 is a central player in controlling cilia morphology and IFT machinery. However, we cannot rule out the possibility of microtubule defects in cilia ultrastructure in *elmd-1;rpi-2* double mutants. Additional work is needed, and a transmission electron microscope (TEM) may be used to reveal further details in the ultrastructure of cilia in these double mutants.

How do these proteins work together to regulate cilia-related phenotypes? While WDR31 is a poorly characterized gene, the roles of human RP2 and ELMOD proteins in cilia biology are better understood. Human RP2 localizes to the cilium and the basal body and displays GAP activity toward two ARF family members, ARL2 and ARL3, both of which were linked to cilia biology (Evans et al., 2010; Schwarz et al., 2017; Wright et al., 2011), while the ELMOD protein family (ELMOD1-3) has GAP activity for ARL2 (ELMOD1 and ELMOD3) and ARF6 (ELMOD1) (Ivanova et al., 2014; Jaworek et al., 2013; Johnson et al., 2012; Miryounesi et al., 2019). ELMOD2 localizes to the basal body, and our study showed ELMOD3 localizes to cilium (Turn et al., 2021). Taking into account the fact that RPI-2 and ELMD-1 are GAPs, and loss of these two GAP proteins likely result in the overactivation of their target G proteins, how does WDR-31 function with these GAP proteins? One possibility is that WDR31 may function downstream of

regulatory GTPases, including ARL2, ARL3, or unidentified GTPases, activated by these GAP proteins. One downside of this explanation is that *wdr-31* single mutants did not have significant ciliary and IFT defects; but, if this were valid, we would expect to observe further anomalies in cilia and IFT in *wdr-31* single mutants, close to the removal of these three genes. Alternatively, the activity/function of overactive GTPases can be somehow regulated by WDR-31, maybe WDR-31 may have a GAP activity for the regulatory GTPases or it may have a GTPase activity. While WDR-31 does not seem to have a GAP domain, HHMER search revealed that human WDR31 has a distant sequence resemblance to a nucleoside-triphosphatase (NTPase) domain (NACHT) containing protein in *Penicillium camemberti* (Gabler et al., 2020). PSI-BLAST search confirmed this result (unpublished data).

Furthermore, the ciliary roles of these two GAP proteins might be independent of their GAP activities, and consistent with this idea, the recent study showed the ciliary roles of ELMOD2 are partially independent of its GAP activity (Turn et al., 2021). However, a variety of evidence suggests that WDR31 and ELMOD3 do not form a complex. First, mass spectrometry-based proteomic analysis for either WDR31 or ELMOD3 showed that neither WDR31 nor ELMOD3 contains each other or RP2 (unpublished data). Second, the proper localization of any of these three proteins was independent of each other (unpublished data). Further studies are needed to understand a mechanistic link between WDR31, ELMOD, and RP2, and figure out the independent contributions of WDR31 and both GAP proteins in cilia biology.

A potential function for WDR31-ELMOD-RP2 in determining the integrity of ciliary gate

Our findings that worm lacking WDR31-ELMOD-RP2 also display ciliary entrance of non-ciliary proteins (TRAM-1) suggests that these proteins may play a function in the ciliary gate. Despite the

mechanism by which these proteins regulate the ciliary gate functions remains unknown, the abnormality of IFT proteins (abnormal distribution and increased anterograde IFT velocities) in triple mutant may provide some hint about the potential roles of these proteins in ciliary gate. One possible explanation is that the IFT defect in triple mutant potentially results in compromised ciliary gate function. Consistent with this possibility, it was previously reported that in *C. elegans,* the elimination of IFT complex A components and cytoplasmic dynein motor CHE-3 result in a defect in ciliary gate function (Jensen et al., 2018; Scheidel and Blacque, 2018).

The WDR31-ELMOD-RP2 is needed for efficient IFT entry and IFT dynamics

Our findings show that simultaneous disruption of *WDR-31*, *ELMD-1*, and *RPI-2* causes differential effects on ciliary IFT protein localizations, including accumulation of IFT-B subcomplex components (IFT-74 and OSM-6), dynein (CHE-3) and kinesin motor (OSM-3) or dim cilia staining of IFT-A subcomplex component and a dynein component (CHE-11 and XBX-1) or almost no cilia entry of a BBSome component (BBS-7). Furthermore, with the exception of cytoplasmic dynein CHE-3, the triple mutant shows a significant decrease in moving IFT particles along cilia in both directions for almost all IFT proteins, indicating that the combined elimination of WDR-31, ELMD-1, and RPI-2 has a significant impact on ciliary recruitment of IFT/BBSome components (IFT-74, OSM-6, CHE-11, and BBS-7) and OSM-3. Our *in vivo* time lapse movie analysis indicated that anterograde IFT velocities for OSM-3, OSM-6, IFT-74, and CHE-11 in the middle segment of cilia are considerably increased in the triple mutant, while IFT velocities in the distal segment of cilia and retrograde direction are unaltered (**Fig. 8A, B, C and D**). This suggests that in cilia lacking *WDR-31, ELMD-1*, or *RPI-2*, certain portions of these IFT proteins are not effectively loaded onto anterograde IFT.

Based on our results, which involve increase in anterograde IFT speed, a decrease in moving IFT particles in anterograde and retrograde transport, ciliary tip aggregation of OSM-3/KIF17 and IFT-B, and failure of docking of BBSome to the IFT machinery, we propose that some of these defects likely stem from the failure of BBSome to associate with moving IFT in cilia in double and triple mutants. These proteins are likely regulator for IFT/BBSome. Consistent with our proposal, the almost comparable IFT/BBSome phenotypes were reported with hypomorphic mutations in *dyf-2* (WDR19 orthologue, an IFT-A component) and *bbs-1* (a BBSome component), where they showed that while BBSome remains at the base of cilia and does not undergo IFT, the failure of IFT-B reassociation with IFT-A at the ciliary tips results in IFT-B ciliary tip accumulations, despite the fact the association of IFT-A and IFT-B components in anterograde transport persists (Wei et al., 2012). They proposed that the BBSome controls the IFT assembly at the ciliary base and IFT turnover at the ciliary tip. However, several of the abnormalities identified in the triple mutant, such as diminished IFT frequencies and ectopic projection from the ciliary base, are unlikely to be related to BBSome dysfunction in the triple mutant, because our findings revealed that the IFT frequency in the *bbs-8* mutant stays intact. Plus, we did not observe ectopic project from the ciliary base in the *bbs-8* mutant (Data not shown).

However, the IFT defects in the triple mutant are unlikely to be due to mislocalization of transition fiber proteins such as DYF-19 (the FBF1 orthologue), which was implicated in regulating the ciliary entry of IFT and BBSome, since our data showed that the localization of DYF-19 was not impaired in the triple mutants (Wei et al., 2013).

On the other hand, the effect on IFT might be direct since RP2 was previously proposed to control the intraflagellar transport protein IFT20 pool in the peri-basal body and trafficking of Kif17 and Kif7 to the ciliary tip (Schwarz et al., 2017). However, several interesting questions

676 have yet to be resolved: what is the mechanism by which WDR-31-ELMD-1-RPI-2 regulates the
677 ciliary entry of the BBSome entry? How does WDR-31-ELMD-1-RPI-2 interact with proteins,
678 including ARL6, that regulate the BBSome recruitment (Jin et al., 2010)? Future study research
679 will help us to understand how these proteins regulate BBSome/IFT trafficking. In summary, this
680 study provides a mechanistic explanation of the function of WDR-31, a new ciliary protein,
681 ELMD-1, and RPI-2 in the regulation of cilia biogenesis and also contributes a new regulator for
682 IFT/BBSome.
683

684 **Acknowledgments**

685 We thank Oliver Blacque, Piali Sengupta, Micheal Leroux, the National BioResource Project
686 (NBRP) in Japan, and the CGC in the United States, which is financed by the NIH Office of
687 Research Infrastructure Programs (P40 OD010440) for sharing valuable strains. We thank Oliver
688 Blacque and Samuel Katz for critical reading of the manuscript. We thank the Abdullah Gul
689 University Scientific Research Project Coordination Unit (Project number: TOA-2018-110) for
690 providing the funding that initiated the project. M.U. was supported by the Tistou & Charlotte
691 Kerstan Stiftung. The Leica laser scanning microscope was funded by a grant from Deutsche
692 Forschungsgemeinschaft (INST 2388/62-1).
693
694
695
696
697

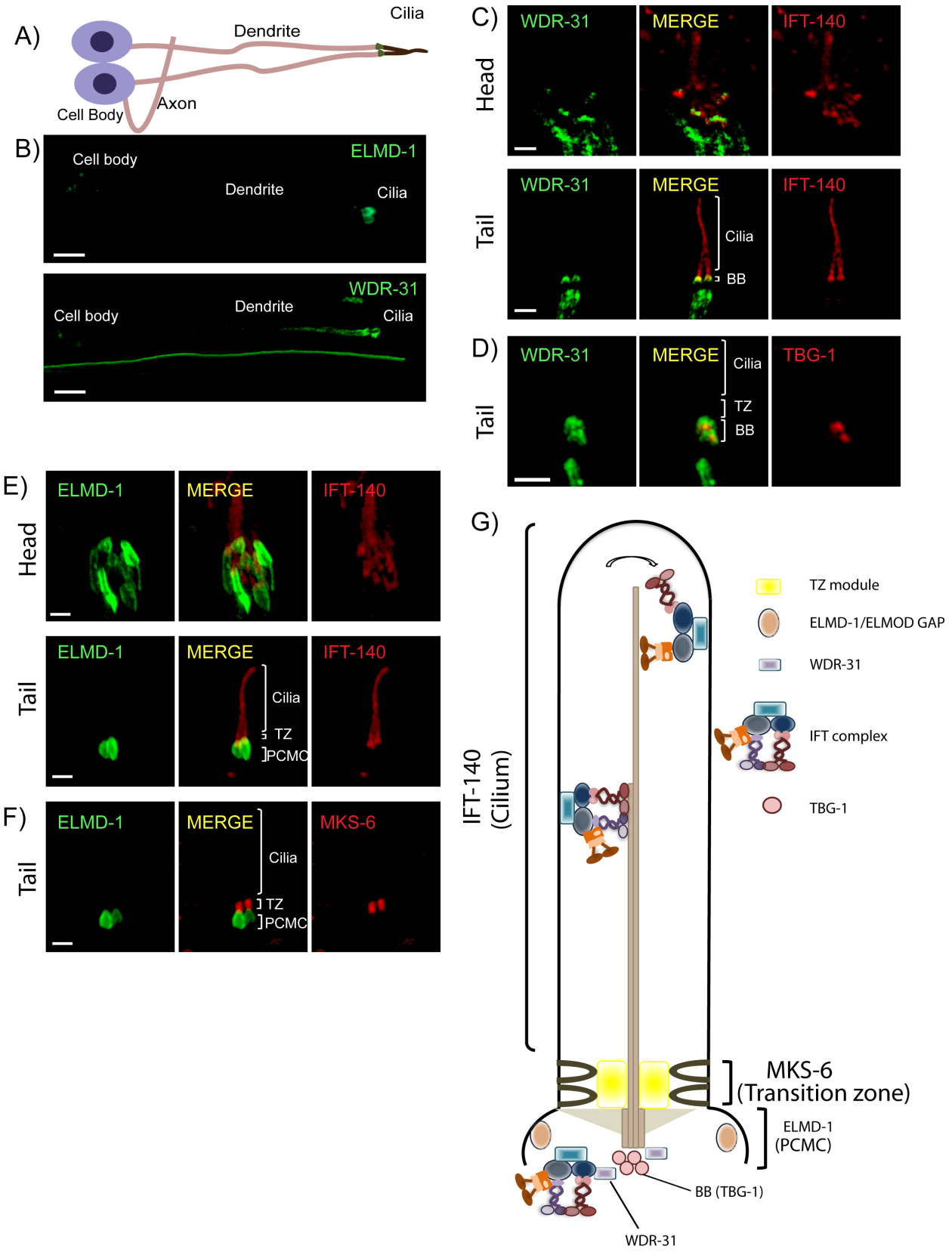

698

699 **Figure 1: WDR-31/WDR31 and ELMD-1/ELMOD proteins are evolutionary conserved**
700 **ciliary proteins A, B)** Shown are the representative drawing of the PHA/PHB sensory neuron
701 (phasmid neurons located in the tail). Cilia, dendrite, axon and cell soma (cell body) are depicted
702 in the drawing. Fluorescence images from the transgenic strain carrying WDR-31::GFP or
703 GFP::ELMD-1 were displayed in the PHA/PHB sensory neurons. Scale bars: 3 μm **C, D)** Co-
704 localization of WDR-31::GFP (Green) with the IFT-140::mCherry (Red, an IFT-A component, a
705 ciliary marker) or TBG-1:mKate (Red, γ-Tubulin, the basal body) in the tail (phasmids) and head
706 (amphid) sensory neurons. TZ and BB denote the transition zone and the basal body, respectively
707 **E, F)** GFP::ELMD-1 (Green) localizes to the BB and PCMC (the periciliary membrane
708 compartment) proximal to the transition zone. Co-labelling of GFP::ELMD-1 with MKS-
709 6:mCherry marker (transition zone) or IFT-140::mCherry in the tail (phasmids) and head (amphid)
710 neurons. Scale bars: 2 μm **G)** Shown are representative localizations of WDR-31 and ELMD-1.
711

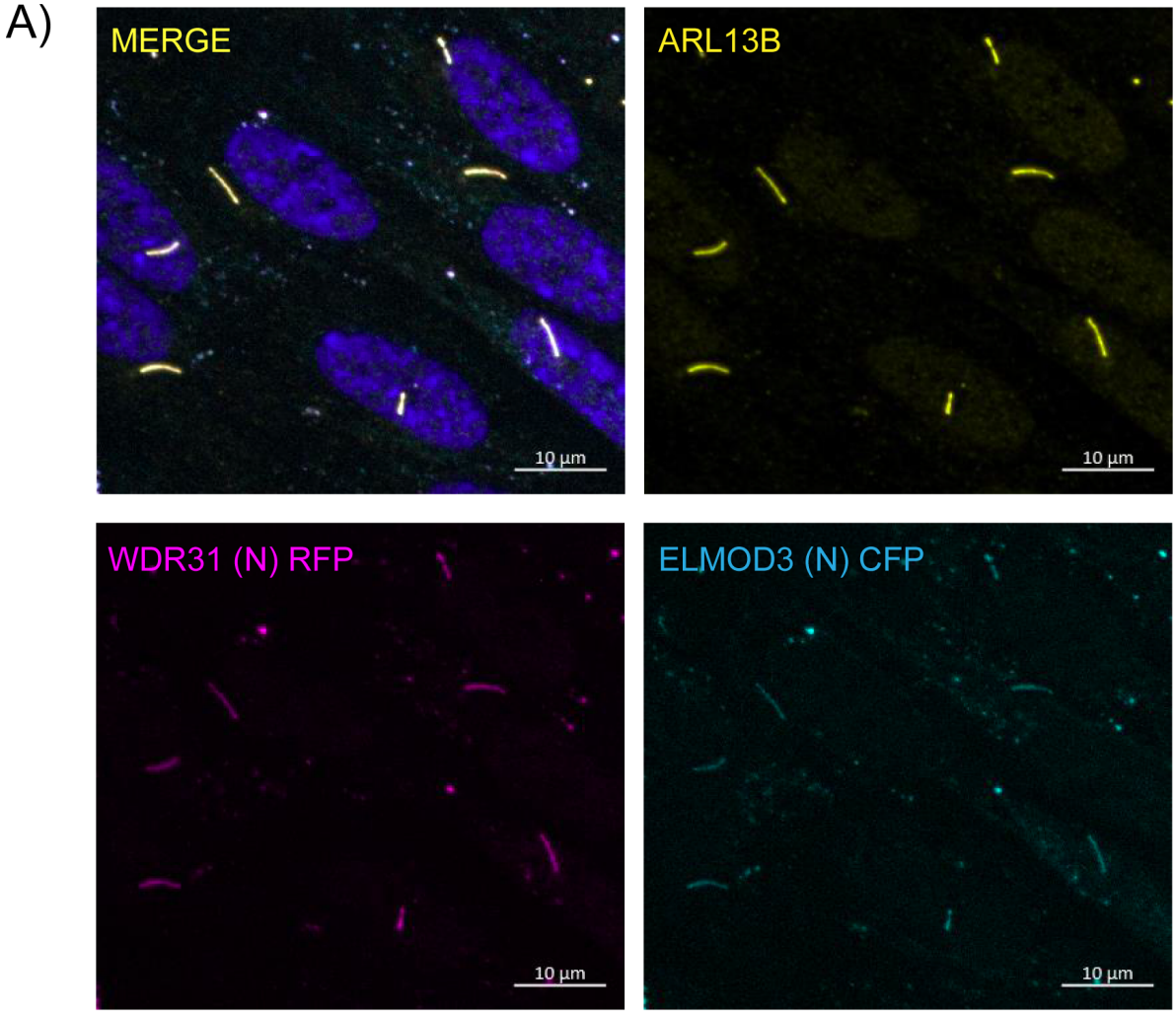

712

713 **Figure 2**: **ELMOD3 and WDR31 localize to the primary cilium**. **A, B**) Shown are the staining
714 of WDR31 (tagged with cyan fluorescent protein) and ELMOD3 (tagged with red fluorescent
715 protein) together with a ciliary marker ARL13B and DAPI (nucleus) in hTERT-RPE1 cells.
716 hTERT-RPE1 cells were transiently transfected with 100 ng of WDR31:CFP and ELMOD3:RFP.
717 Scale bars: 10 µm (A) and 3 µm (B)
718

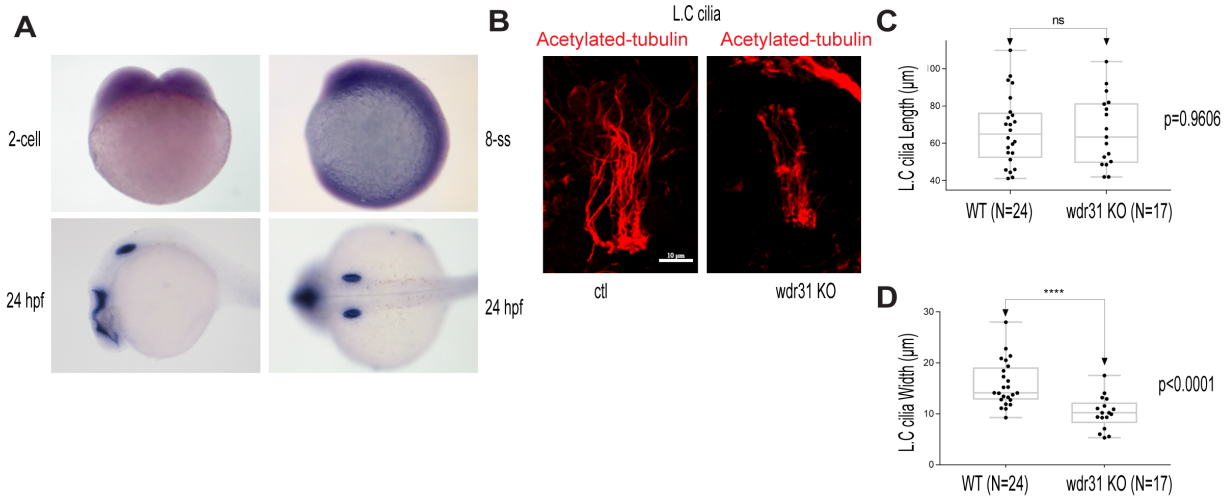

719

720 **Figure 3: WDR31 regulates ciliogenesis in zebrafish A)** Shown are the expression pattern
721 analysis of WDR31 in zebrafish embryos. *Wdr31* is ubiquitously expressed before the
722 segmentation stage (2 cell and 8 somite stages (SS). The expression of *Wdr31* becomes limited to
723 the otic vesicle and brain region at 24 hours post fertilization (24 hpf). **B)** Shown are cilia of lateral
724 crista (LC) of the otic vesicle, stained with acetylated-tubulin, in wild type and *Wdr31* knockout,
725 generated via CRISPR/Cas9. **C and D**) The length of cilia in the lateral crista (LC) of the otic
726 vesicle remains unaffected in zebrafish *Wdr31* knockout while the cilia number is decreased, as
727 shown with the measurement of width of cilia lateral crista (LC) of the otic vesicle.
728
729

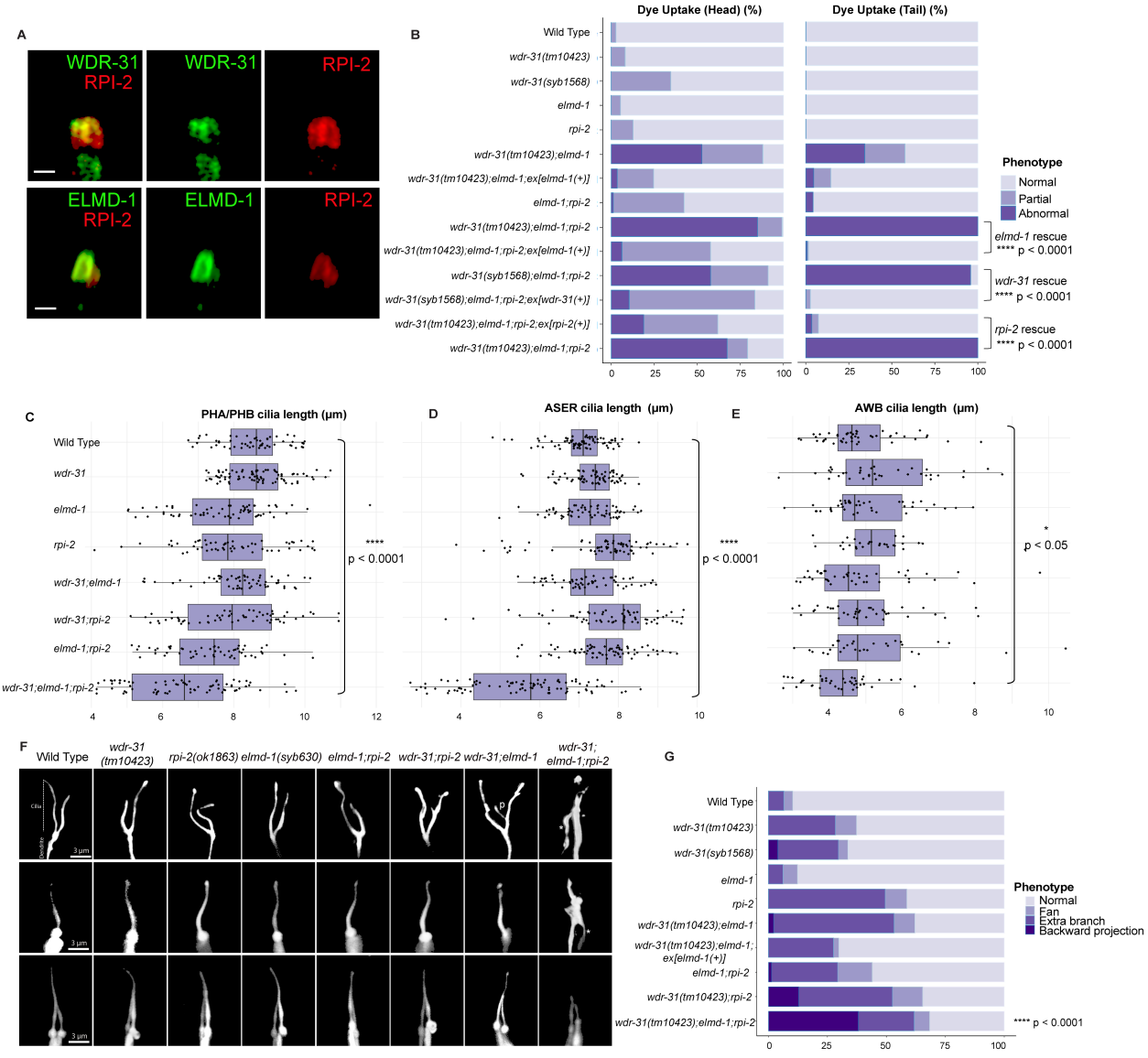

730

731 **Figure 4: WDR31-ELMOD-RP2 are needed for determining cilia length and morphology in**

732 ***C. elegans***

733 **A)** Shown are co-localizations of RPI-2::mCherry (red, the endogenously labeled RPI-2) with

734 either WDR-31::GFP (green, the endogenously labeled WDR-31) or GFP::ELMD-1 (green,

735 overexpressed) in tail (phasmid) sensory neurons in *C. elegans.* Scale bars: 1 μm. **B)** The fraction

736 of the dye uptake defects is presented in bar charts for wild type and the indicated mutants. Fisher's

737 exact test was performed for statistical analysis between indicated triple mutants and a rescue gene

738 for Dye assay. Brackets show statistical significance between two strains compared ($p < 0.0001$
739 and **** indicate statistical significance). **C, D, E)** Shown is the jitter plot for PHA/PHB cilia,
740 ASER cilia and AWB short cilia length (μm) for wild type and indicated mutant strains. Statistical
741 significance between wild type and triple mutants was shown with bracket. **** implies statistical
742 significance which means that p value is lower than $p < 0.0001$ while * means that p value is lower
743 than $p < 0.05$. **F)** Fluorescence images show the morphology of AWB cilia (fork-like structure
744 located in the head), ASER cilia (amphid channel cilia) and PHA/PHB cilia (phasmid channel
745 cilia) in wild type and indicated mutant backgrounds. The backward projection from the cilia is
746 shown with asterisks (*) while p indicates the ectopic projections from the middle parts of cilia.
747 Scale bars: 3 μm **G)** The percentage of the abnormality in AWB cilia morphology is depicted in
748 bar charts. Fisher's exact test was utilized for statistical analysis of AWB cilia morphology between
749 wild type and designated mutants, and **** denotes statistical significance.
750

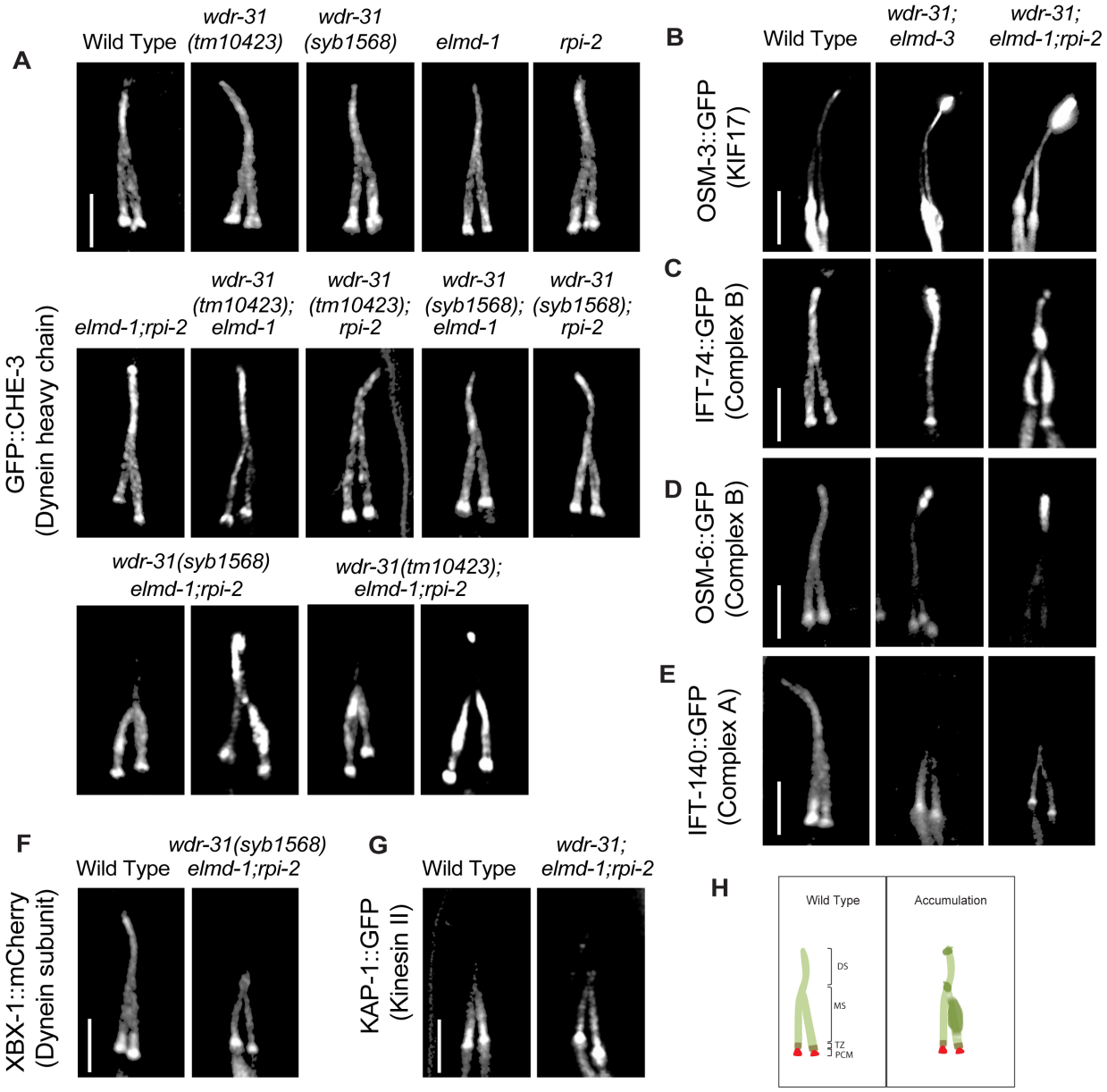

751

752 **Figure 5: IFT-B proteins and OSM-3/KIF17 accumulate at the ciliary tip.** Shown are
753 fluorescent images of PHA/PHB cilia (phasmid tail). **A)** Fluorescent images from a single copy
754 GFP::CHE-3 (human dynein heavy chain DYNC2H1) in wild type and indicated mutant
755 backgrounds are displayed. GFP::CHE-3 accumulations within cilia and dim distal cilia staining

were observed in two distinct triple mutants (*wdr-31(tm10423);elmd-1;rpi-2* and *wdr-31(syb1568);elmd-1;rpi-2).* Scale bars: 3 μm **B, C, D, E, F)** Confocal microscopy analysis of IFT-A (IFT-140::GFP) and IFT-B complex components (OSM-6/IFT52::GFP and IFT-74::GFP) revealed differential abnormalities in the transport of IFT-A and IFT-B components in double (w*dr-31;elmd-1*) and triple mutants. The localization of XBX-1::mCherry (Dynein subunit) in *wdr-31(syb1568);elmd-1;rpi-2* triple mutants phenocopies the dim distal cilia staining of IFT-A (IFT-140::GFP) in the w*dr-31(tm10423);elmd-1;rpi-2* triple mutants. OSM-3/KIF17 Kinesin motor accumulates at the ciliary tips in w*dr-31(tm10423);elmd-1* double and w*dr-31(tm10423);elmd-1;rpi-2* triple mutants. Compared to double mutants, the ciliary tip staining is stronger in the triple mutants. Scale bars: 3 μm **G)** Fluorescent images from Kinesin II motor (KAP-1::GFP) revealed that the restricted middle segment localization of KAP-1 remains unchanged in w*dr-31(tm10423);elmd-1;rpi-2* triple mutants. Scale bars: 3 μm **H)** Shown are the drawings of phasmid cilia (PHA/PHB sensory neurons in the tail) in wild type and mutants showing ciliary accumulations.

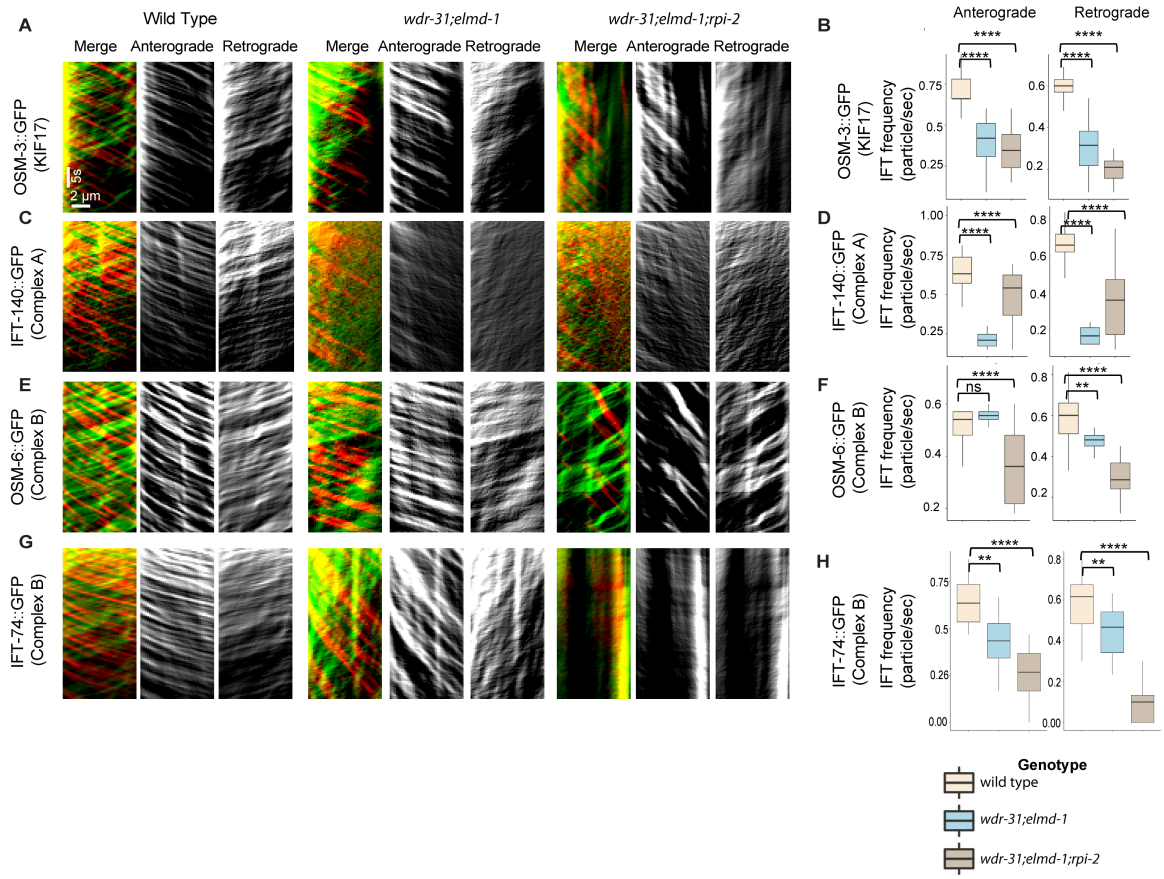

Figure 6: Measurement of anterograde and retrograde IFT transport frequency A, C, E and G) Shown are representative kymographs of GFP tagged IFT proteins translocating in the tail cilia (PHA/PHB sensory neurons) of wild type and indicated mutants. Kymographs for anterograde, retrogrades and merged (Red & Green) were generated with ImageJ equipped with KymographClear. The trajectory represents a moving IFT particle, and the average number of moving IFT particles in wild type and indicated mutants (double, triple) was calculated by counting all trajectories in each kymograph. Travel time and distance are shown on kymographs. **B, D, F and H)** Box-and-Whisker charts with error bars were created to visualize the average number of IFT anterograde and retrograde particles between wild type and indicated mutants. The Mann–Whitney U test was used to measure statistical analysis and significance. The four and three

asterisks (**** and ***) at the top of the brackets indicate that the p value between the two strains is less than 0.0001 and 0.001, respectively, suggesting statistical significance. Ns stands for "not significant."

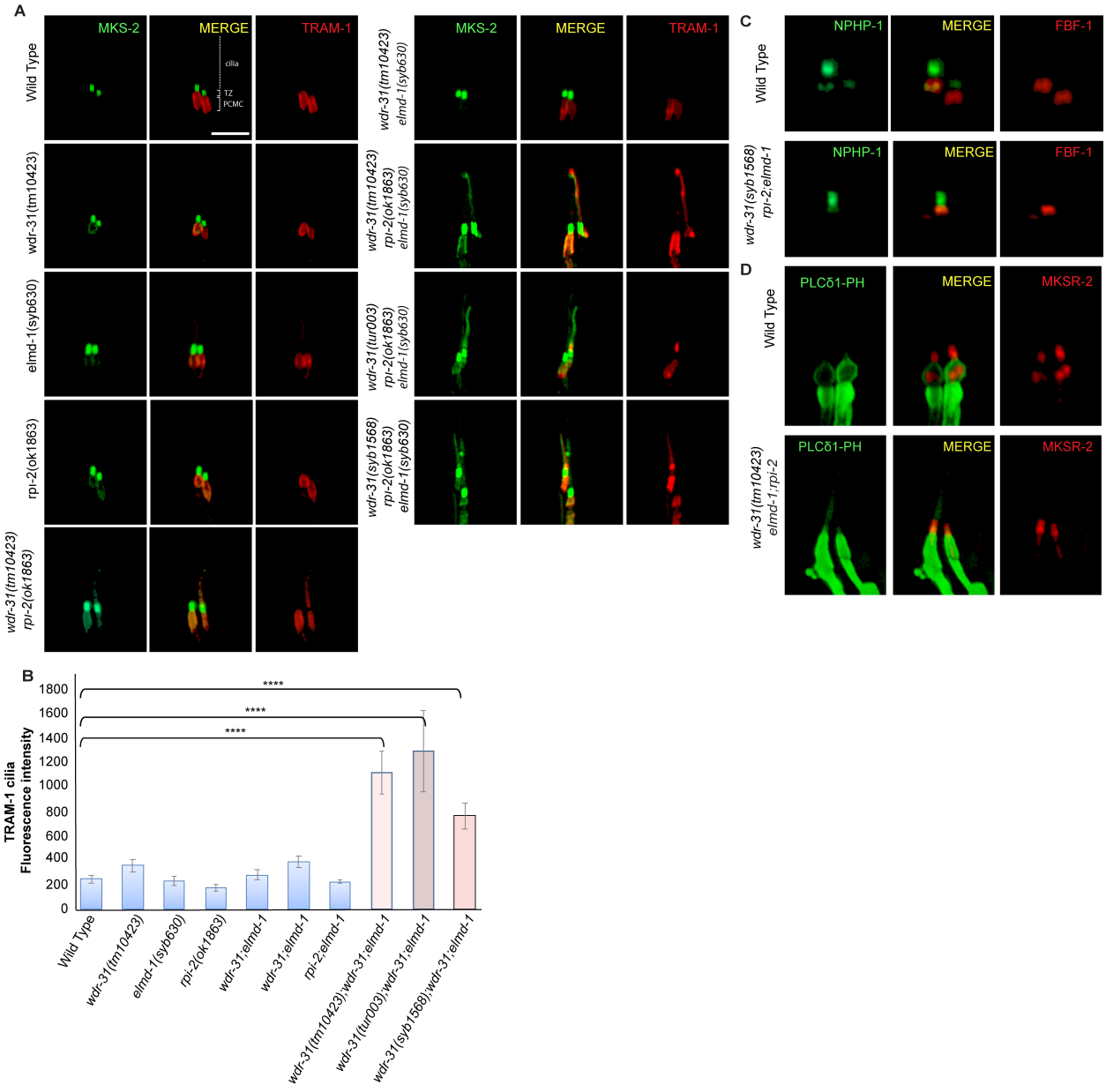

Figure 7: A non-ciliary membrane protein TRAM-1 enters into cilia in *wdr-31;elmd-1;rpi-2* triple mutants. A) Confocal fluorescent images exhibit the localization of tdTomato tagged

798 TRAM-1 (a PCMC marker) and MSK-2::GFP (a TZ marker) in wild type and indicated mutants.
799 TRAM-1 leaks into cilia in all three *wdr-31* triple mutants. Cilia, the periciliary membrane
800 compartment (PCMC), and transition zone (TZ) are depicted in the fluorescent image. Scale bars:
801 2 μm, **B)** TRAM-1 fluorescence intensities in cilia were measured in wild type and designated
802 mutants, and the results were shown in the plot. The four asterisks (****) indicate statistically
803 significant differences between the wild type and the identified triple mutants. **C)** The localization
804 of NPHP-1::GFP (a transition zone protein) and FBF-1::mCherry (a transition fiber protein) was
805 similar unaffected in *wdr-31;elmd-1;rpi-2* triple mutants **D)** The PLCδ1-PH::GFP (a marker for
806 monitoring phosphatidylinositol 4,5-bisphosphate (PtdIns(4,5)P2) in the plasma membrane)
807 decorates the membranes of PCMC and does not enter into cilia in wild type. MKSR-2 was used
808 to mark the transition zone. The PLCδ1-PH::GFP stays outside of cilia in the *wdr-31;elmd-1;rpi-*
809 *2* triple mutants.
810
811

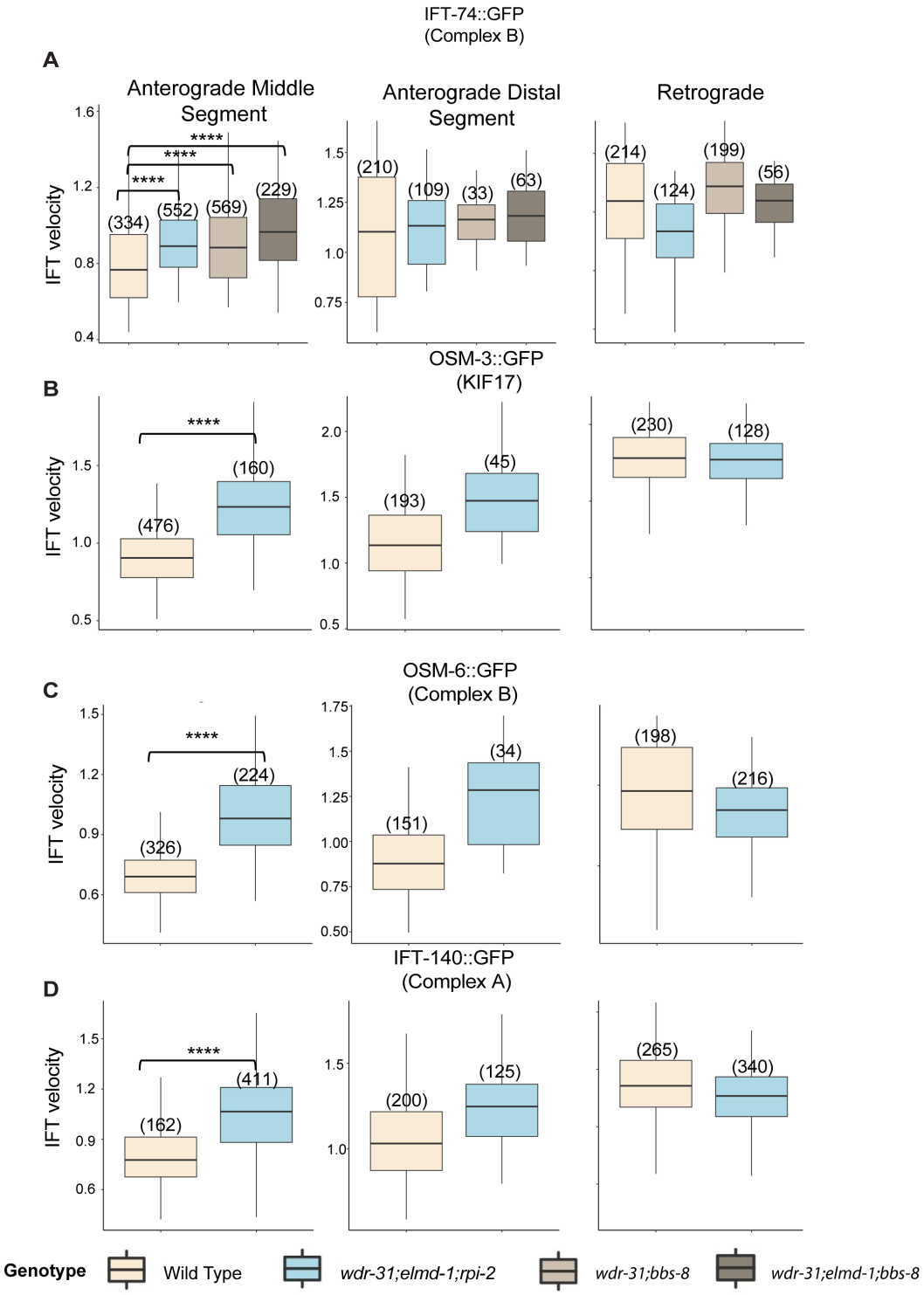

812

Figure 8: The average anterograde IFT velocities were significantly increased in *wdr-13;elmd-1;rpi-2* triple mutants, A, B, C, and D) The average anterograde (distal and middle segments) and retrograde IFT velocities were calculated, and box-and-whisker plots with error bars were used to depict them. Numbers shown at the top of bars represent the number of IFT particles used for determining IFT velocities. To compare statistical analysis and significance between wild type and specified mutations, the Mann–Whitney U test was performed. A p value of less than 0.0001 indicates statistical significance between the two strains, as shown by the four asterisks (****) at the top of the brackets.

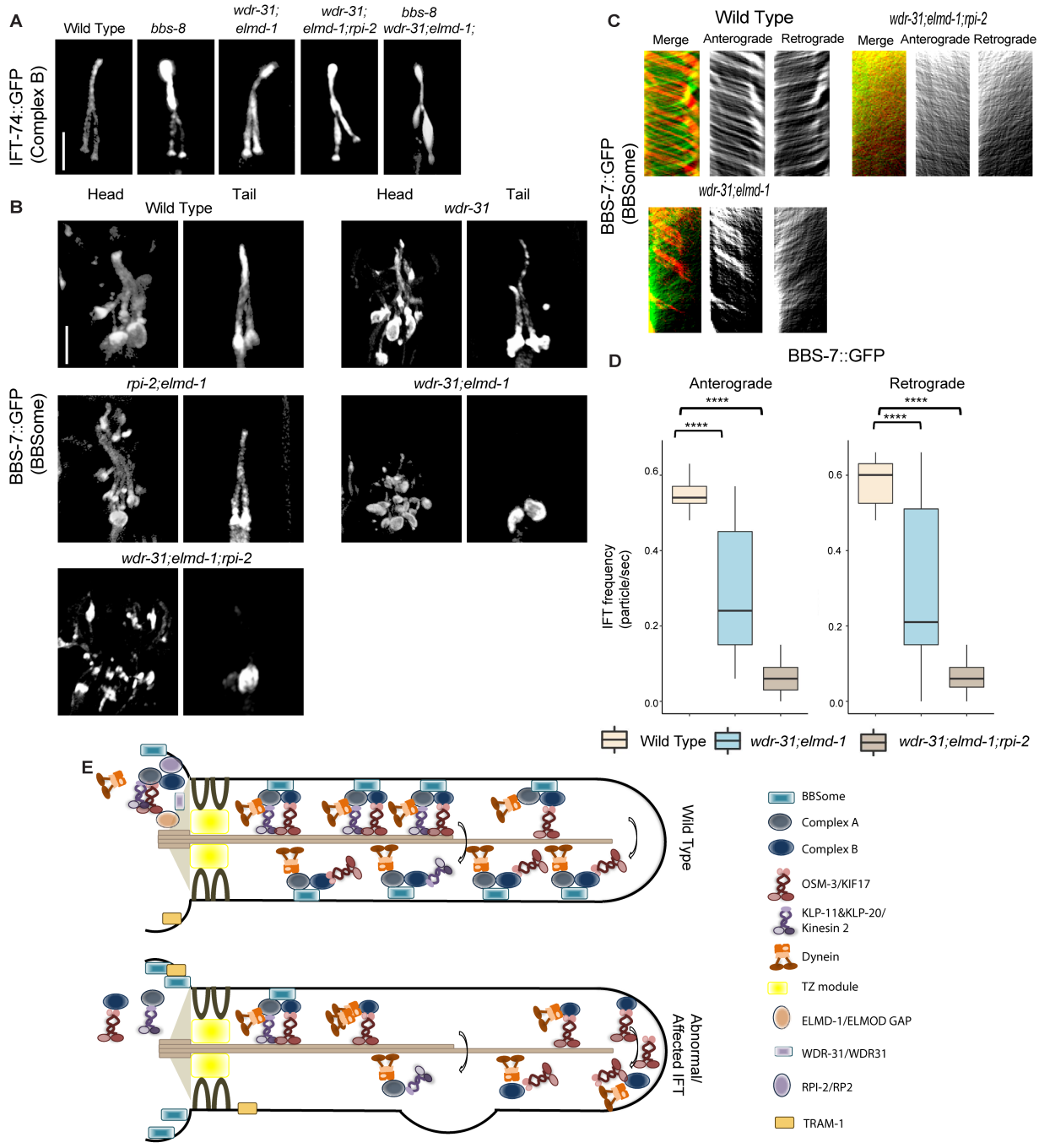

Figure 9: WDR-31 and ELMD-1 regulate the recruitment of BBSome to cilia.

A) Shown are fluorescence images from the transgenic strain carrying IFT-74::GFP, an IFT-B component, in wild type, *wdr-31;elmd-1* double mutants, *wdr-31;elmd-1;rpi-2* and *wdr-31;elmd-1;bbs-8* triple mutants, and *bbs-8(nx77).* The IFT-B subunit IFT-74:GFP accumulates at the ciliary

827 tips and cilia in the tail of all three mutants. **B)** Confocal fluorescence images showing the
828 localization of BBS-7:GFP, a BBSome subunit, in the heads and tails of wild type and *wdr-*
829 *31(tm10423); wdr-31;elmd-1*; *rpi-2;elmd-1* double and *wdr-31;elmd-1;rpi-2* triple mutants.
830 Fluorescence images showed absent or weak cilia staining of BBS-7::GFP in both the head and
831 tails of *wdr-31;elmd-1* and *wdr-31;elmd-1;rpi-2* triple mutants. **C)** Kymographs were created from
832 time-lapse BBS-7::GFP movies (PHA/PHB cilia) using KymographClear integrated into ImageJ.
833 Shown are representative kymographs for BBS-7::GFP translocating in wild type and indicated
834 mutants. Each trajectory in kymographs was counted. Travel time and distance are included on
835 kymograph **D)** The graph depicts the average number of BBS-7::GFP particles traveling around
836 cilia in both directions for wild type and indicated mutants. The Mann–Whitney U test revealed
837 statistical significance between the compared strains and that the p value was less than 0.0001
838 shown by the four asterisks (****) at the top of the brackets **E)** In wild type, the assembly of the
839 Kinesin-IFT-BBSome complex (Kinesin-II and OSM-3**,** IFT-B , IFT-A and BBSome) happens at
840 the base of cilia. In the middle segment of amphid and phasmid cilia in *C. elegans*, both
841 heterotrimeric Kinesin II and homodimeric OSM-3 transport the IFT-A- IFT-B- BBSome complex
842 in an anterograde direction. Heterotrimeric Kinesin II returns to the ciliary base when it reaches
843 the tip of the middle segment of amphid and phasmid cilia, whereas homodimeric OSM-3 is
844 responsible for the anterograde translocation of the IFT-BBSome complex in the distal segment of
845 amphid and phasmid cilia. When the OSM-3-IFT-BBSome complex reaches the ciliary tip,
846 cytoplasmic dynein transports them back to the ciliary base. In *wdr-31;elmd-1* double *wdr-*
847 *31;elmd-1;rpi-2* triple mutants, the BBSome failed to enter into cilia, thus leading to accumulations
848 of OSM-3 and IFT-B components in the ciliary tips.
849

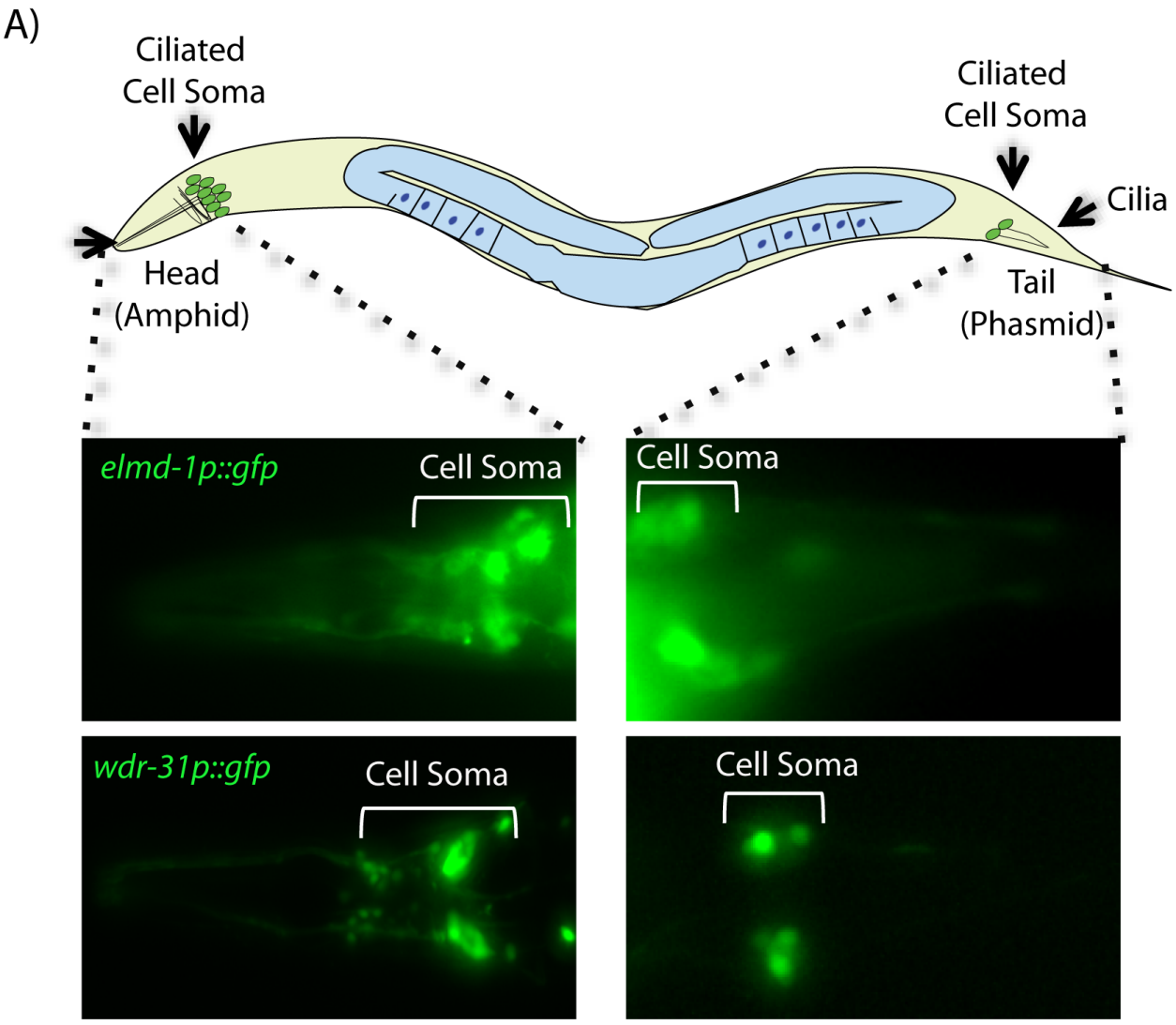

Supplementary Figure 1: Expression patterns of WDR-31 and ELMD-1. A) A total of 60 sensory neurons are distributed in the head (amphid) and tails (phasmid) of *C. elegans.* The ciliated sensory neurons are displayed in the schematic of *C. elegans.* The expression of *elmd-1promoter::gfp* (1000 kb) and *wdr-31promoter::gfp* (1000 kb) were shown in the fluorescence images. The cell of ciliated sensory neurons (cell soma) in the head and tails were displayed in brackets.

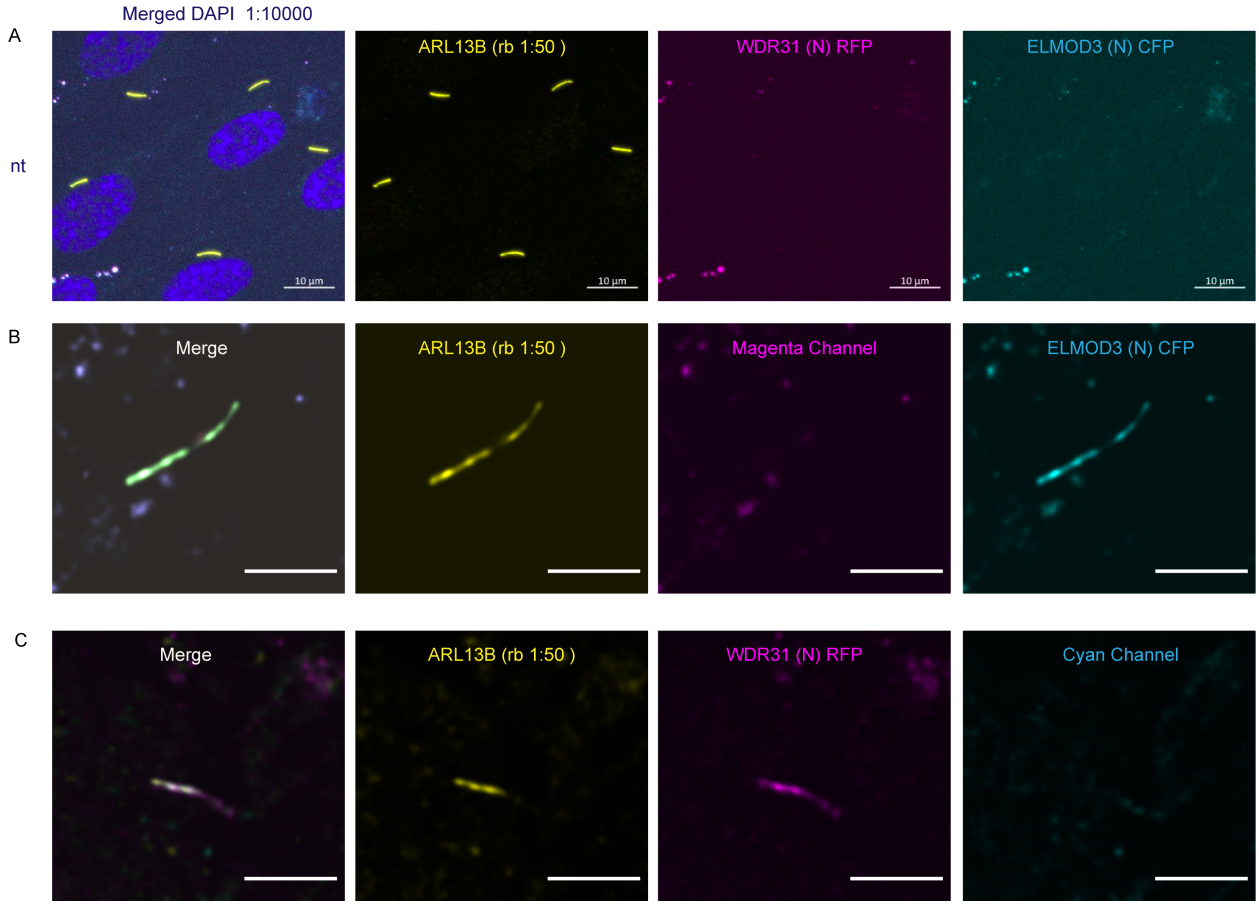

Supplementary Figure 2: Ciliary localization of WDR31 and ELMOD3 in hTERT-RPE1 cells A) Images showing immunostaining of a ciliary marker ARL13B and DAPI (nucleus) in hTERT-RPE1 cells. NT represents no transfection of hTERT-RPE1 with WDR31 (tagged with cyan fluorescent protein) and ELMOD3 (tagged with red fluorescent protein). Scale bars: 10 µm. **B)** Images showing immunostaining of hTERT-RPE1 cells transfected with ELMOD3-CFP (cyan) and also stained for ARL13B (yellow). The magenta channel only shows some background but no localization to the cilium. Green regions in the "merge" picture show co-localization of both ELMOD3 and ARL13B proteins. Scale bars: 3 µm. **C)** Fluorescence images displaying hTERT-RPE1 Fluorescence images of immunostaining for ARL13B (yellow) and WDR31-RFP (magenta) in hTERT-RPE1 cells transfected with WDR31-RFP (cyan). The cyan channel shows some

870 background, with no cilium localisation. WDR31 and ARL1B proteins are co-localized in the pink

871 sections of the "merge" image. Scale bars: 3 μm.

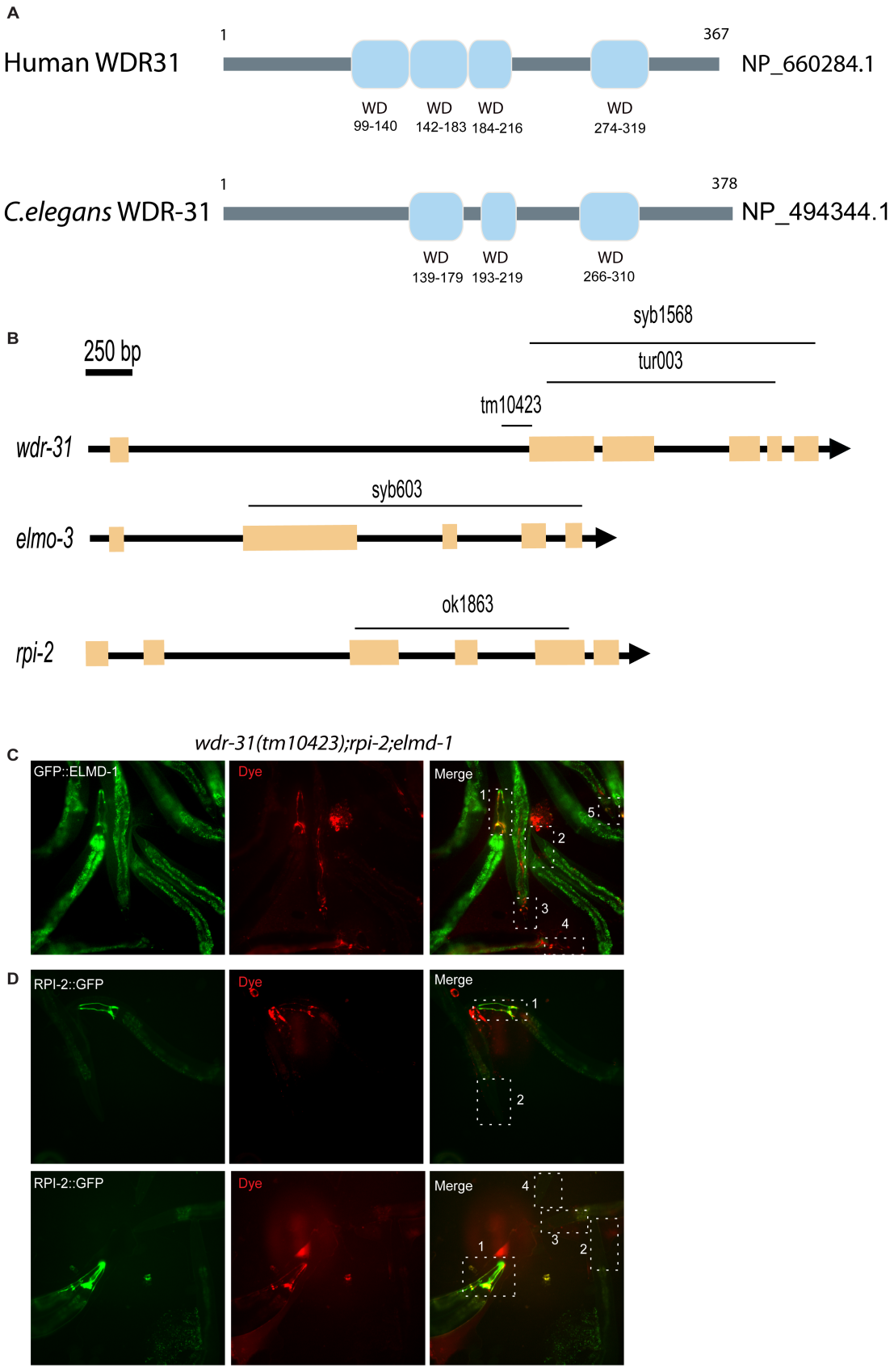

872

Supplementary Figure 3: Rescue of dye uptake defects by ELMD-1 or RPI-2.

A) Shown are representative schematics of human and *C. elegans* WDR-31/WDR31. Human WDR31 (NP_660284.1) has four WD domains while *C. elegans* WDR-31 (NP_494344.1) has three WD domains (https://prosite.expasy.org/; Sigrist CJA et al 2012). **B)** Schematic diagrams of *wdr-31*, *elmd-1* and *rpi-2* together with corresponding deletions are shown. Scale bars: 250 bp. **C and D**) Fluorescence microscope images of mutant worms (head and tail) with red-fluorescent dye uptake (texas red filter) and GFP-tagged ELMD-1 and RPI-2 (fluorescence filter set for GFP) are shown. The head or tail in the dotted lines is indicated by numbers in the combined fluorescence images. GFP expression in combination with RED fluorescence indicates the rescue of dye uptake defects.

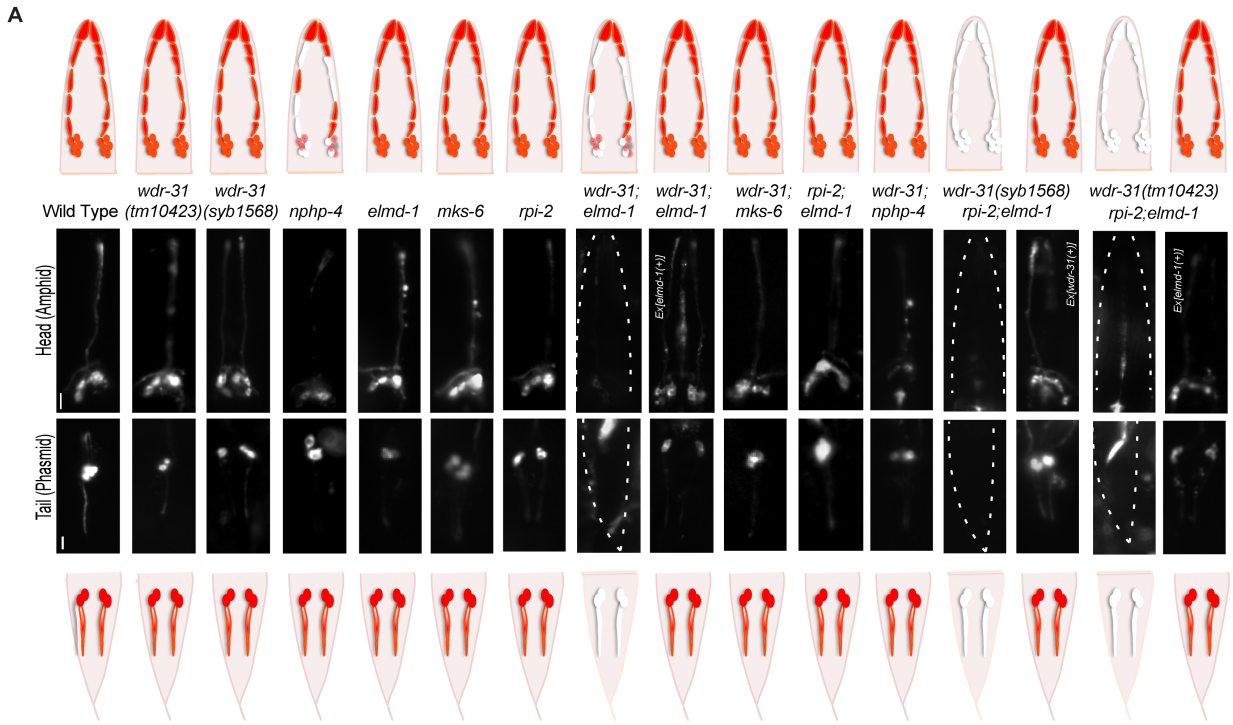

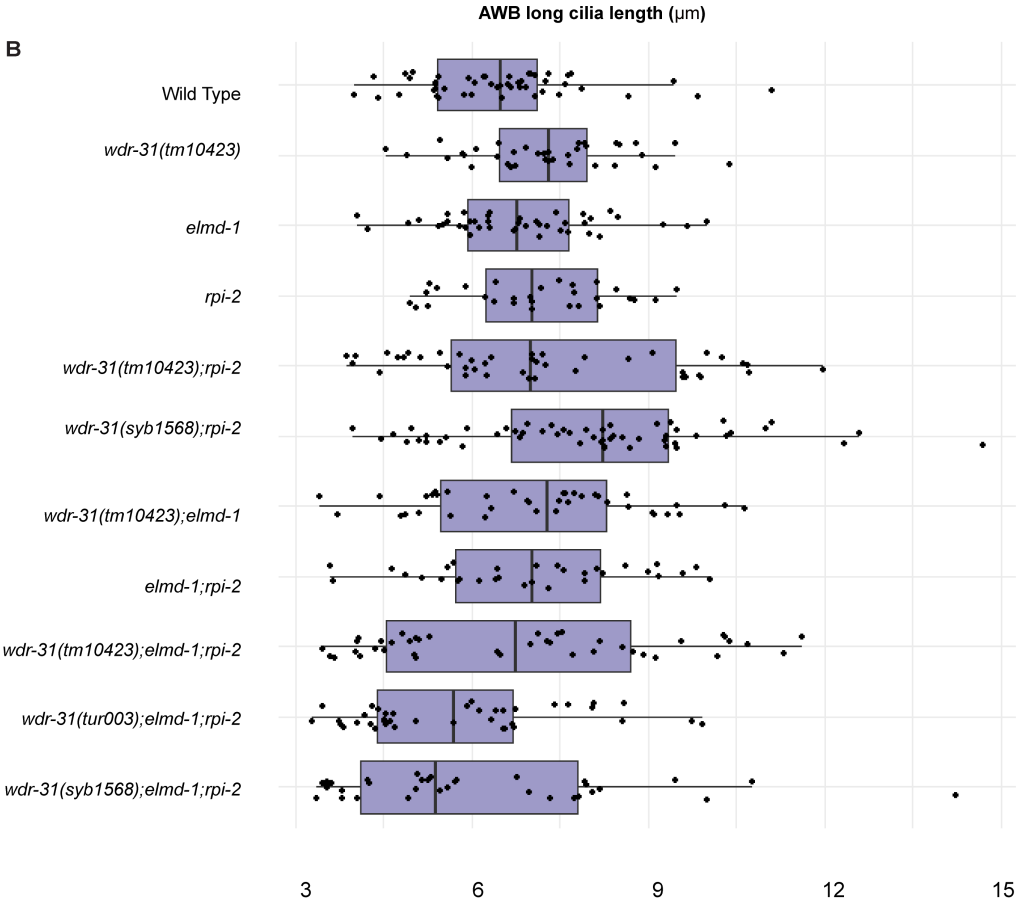

883

Supplementary Figure 4: AWB cilia morphology in WDR-31-ELMD-1-RPI-2 triple mutants

A) Shown are the schematic representations of lipophilic fluorescent dye uptake in the head (amphid) and tail (phasmid) sensory neurons in *C. elegans.* Red labelling indicates the normal dye uptake while the failure of Dye uptake was shown in white. Fluorescence images show the dye update in the head and tail neurons in the wild type and indicated mutant strains. No dye uptake was observed in both head (amphid) and tail (phasmid) of *wdr-31(tm10423);elmd-1* double mutants, *wdr-31(tm10423);elmd-1;rpi-2* and *wdr-31(syb1568);elmd-1;rpi-2* triple mutants. *Ex[elmd-1(+)*] rescues the dye uptake defects of *wdr-31(tm10423);elmd-1* double and *wdr-31(tm10423);elmd-1;rpi-2* triple mutants, while *Ex[wdr-31(+)]* rescues the Dye uptake defects of *wdr-31(syb1568);elmd-1;rpi-2* triple mutants. Scale bars: 10 μm. **B)** Shown is the jitter plot for AWB long cilia length (μm) in wild type and mutant strains.

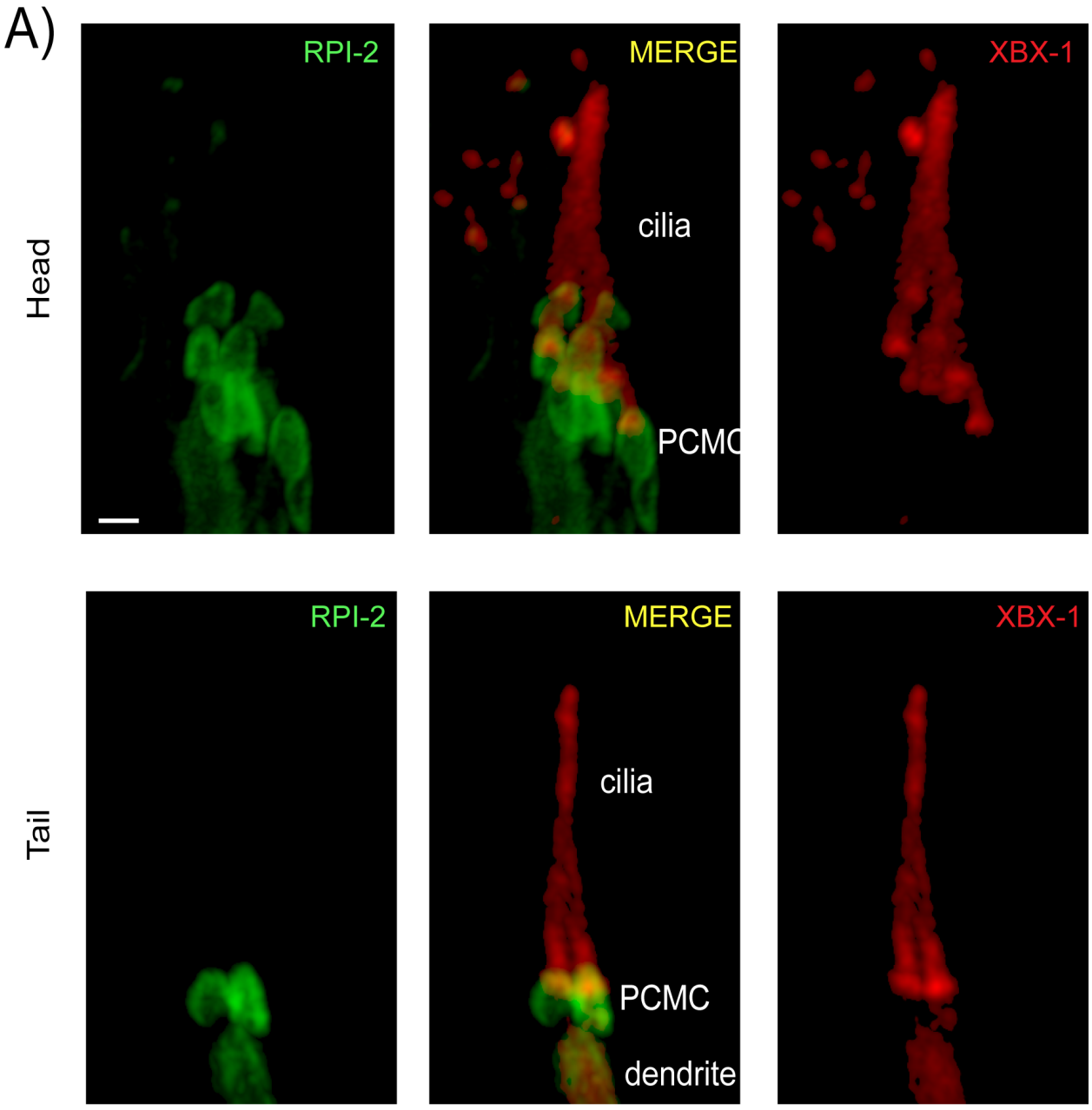

Supplementary Figure 5: A) Shown is co-localization of RPI-2::GFP (human RP2) and XBX-1::mCherry (human DYNC2LI1) in the head and tail sensory neurons. XBX-1 stains the entire cilium and is used as a ciliary marker while RPI-2 is located at PCMC. PCMC denotes the periciliary membrane compartment.

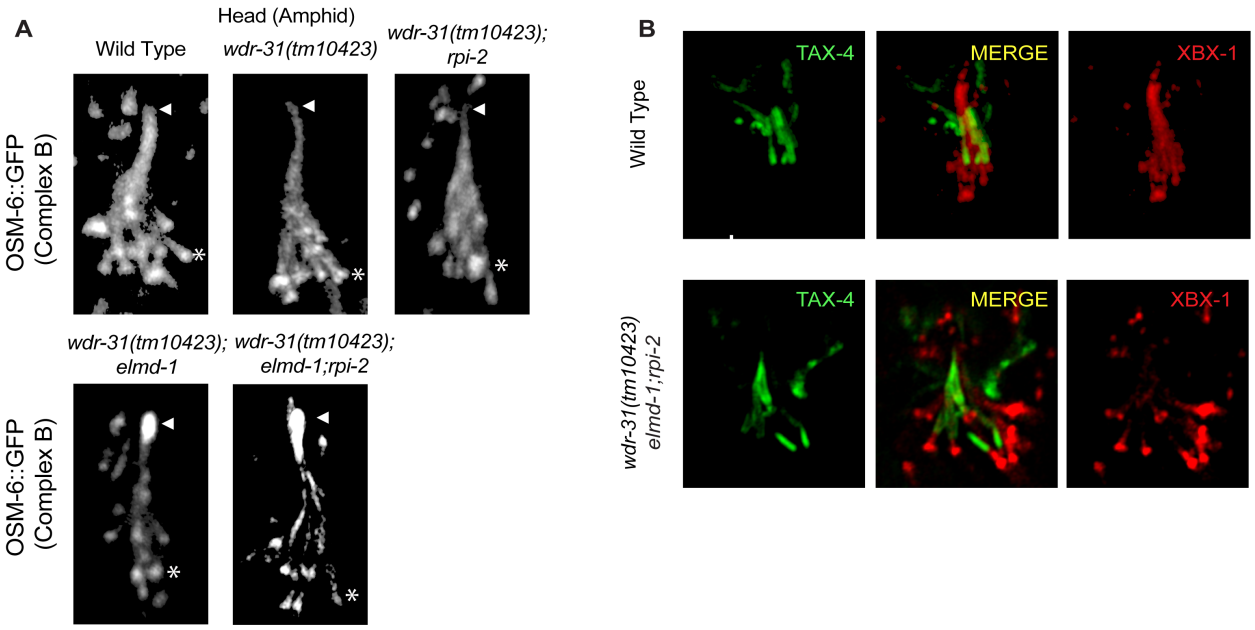

902

903 **Supplementary Figure 6: A)** Confocal images (Z-stack) display the localization of OSM-6::GFP
904 (a single copy transgene, huma IFT52) in the head (a bunch of cilia) of wild type and indicated
905 mutants. Arrow points the ciliary tips while asterisks indicate the ciliary base. **B)** Confocal images
906 show colocalization of TAX-4 (a ciliary membrane protein) and XBX-1::tdTomato (a cilia
907 marker).

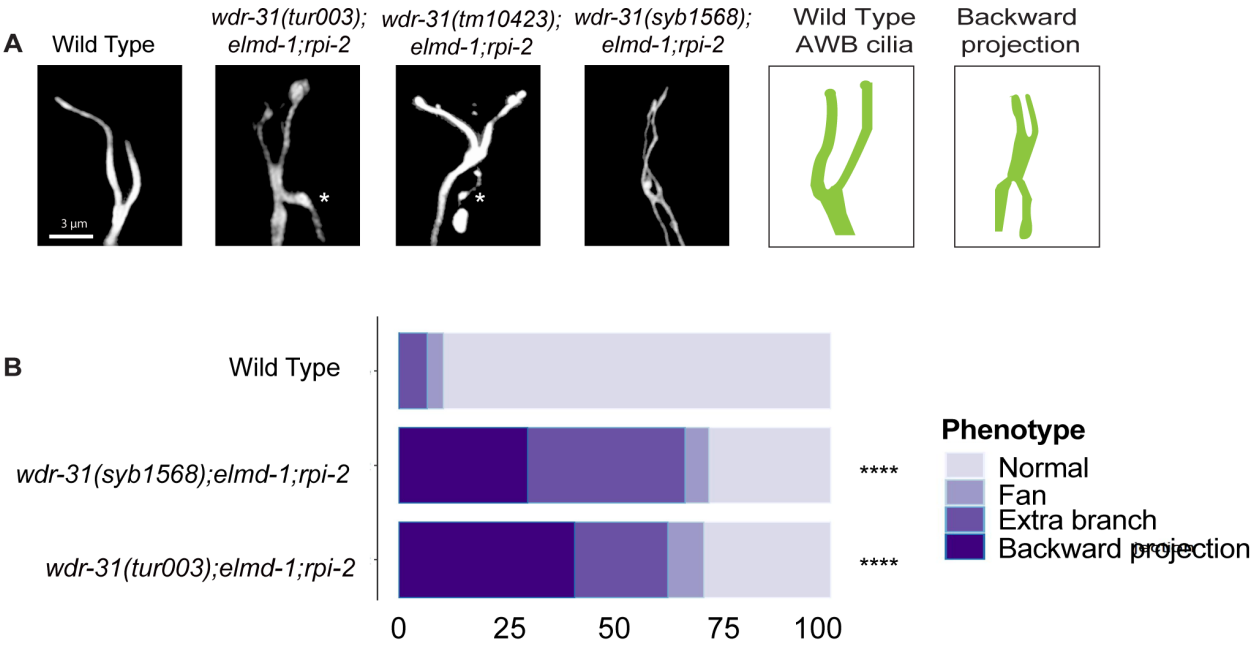

908

Supplementary Figure 7: **A)** The architecture of AWB cilia (a fork-like structure in the head) in wild type and mutant backgrounds is shown in fluorescent images. In schematic illustrations, the AWB cilia in wild type and altered mutants are illustrated. **B)** Shown are bar plots displaying percentage of phenotypes in wild type and indicated triple mutants. Four asterisks (****) indicates statistical significances between wild type and indicated triple mutants.

Supplementary Movies

For the IFT assay, time-lapse movies (3 frames per second) were generated with Leica DM6, and were processed with Image J to generate GIFs (10 fps).

Supplementary Movies:

Supplementary Movie 1: IFT-74::GFP in wild type and indicated mutant backgrounds.

Supplementary Movie 2: OSM-6::GFP in wild type and indicated mutant backgrounds.

Supplementary Movie 3: OSM-3::GFP in wild type and indicated mutant backgrounds

Supplementary Movie 4: GFP::CHE-3 in wild type and indicated mutant backgrounds.

Supplementary Movie 5: IFT-140::GFP in wild type and indicated mutant backgrounds.

Supplementary Movie 6: BBS-7::GFP in wild type and indicated mutant backgrounds.

References

Ansley, S.J., Badano, J.L., Blacque, O.E., Hill, J., Hoskins, B.E., Leitch, C.C., Chul Kim, J., Ross, A.J., Eichers, E.R., Teslovich, T.M., Mah, A.K., Johnsen, R.C., Cavender, J.C., Alan Lewis, R., Leroux, M.R., Beales, P.L., Katsanis, N., 2003. Basal body dysfunction is a likely cause of pleiotropic Bardet–Biedl syndrome. Nature 425, 628–633. https://doi.org/10.1038/nature02030

Anvarian, Z., Mykytyn, K., Mukhopadhyay, S., Pedersen, L.B., Christensen, S.T., 2019. Cellular signalling by primary cilia in development, organ function and disease. Nat. Rev. Nephrol. 15, 199–219. https://doi.org/10.1038/s41581-019-0116-9

Arnaiz, O., Malinowska, A., Klotz, C., Sperling, L., Dadlez, M., Koll, F., Cohen, J., 2009. Cildb: a knowledgebase for centrosomes and cilia. Database 2009. https://doi.org/10.1093/database/bap022

939 Avidor-Reiss, T., Maer, A.M., Koundakjian, E., Polyanovsky, A., Keil, T., Subramaniam, S.,
940 Zuker, C.S., 2004. Decoding Cilia Function. Cell 117, 527–539.
941 https://doi.org/10.1016/S0092-8674(04)00412-X
942
943 Blacque, O., E., 2008. Intraflagellar transport: from molecular characterisation to mechanism.
944 Front. Biosci. 13, 2633. https://doi.org/10.2741/2871
945
946 Blacque, O.E., 2004. Loss of C. elegans BBS-7 and BBS-8 protein function results in cilia
947 defects and compromised intraflagellar transport. Genes Dev. 18, 1630–1642.
948 https://doi.org/10.1101/gad.1194004
949
950 Blacque, O.E., Li, C., Inglis, P.N., Esmail, M.A., Ou, G., Mah, A.K., Baillie, D.L., Scholey,
951 J.M., Leroux, M.R., 2006. The WD Repeat-containing Protein IFTA-1 Is Required for
952 Retrograde Intraflagellar Transport. Mol. Biol. Cell 17, 5053–5062.
953 https://doi.org/10.1091/mbc.e06-06-0571
954
955 Blacque, O.E., Perens, E.A., Boroevich, K.A., Inglis, P.N., Li, C., Warner, A., Khattra, J., Holt,
956 R.A., Ou, G., Mah, A.K., McKay, S.J., Huang, P., Swoboda, P., Jones, S.J.M., Marra,
957 M.A., Baillie, D.L., Moerman, D.G., Shaham, S., Leroux, M.R., 2005. Functional
958 Genomics of the Cilium, a Sensory Organelle. Curr. Biol. 15, 935–941.
959 https://doi.org/10.1016/j.cub.2005.04.059
960
961 Blacque, O.E., Sanders, A.A., 2014. Compartments within a compartment: What *C. elegans* can
962 tell us about ciliary subdomain composition, biogenesis, function, and disease.
963 Organogenesis 10, 126–137. https://doi.org/10.4161/org.28830
964
965 Bloodgood, R.A., 2009. From Central to Rudimentary to Primary: The History of an
966 Underappreciated Organelle Whose Time Has Come.The Primary Cilium, in: Methods in
967 Cell Biology. Elsevier, pp. 2–52. https://doi.org/10.1016/S0091-679X(08)94001-2
968
969 Brenner, S., 1974. The genetics of Caenorhabditis elegans. Genetics 77, 71–94.
970
971 Breslow, D.K., Hoogendoorn, S., Kopp, A.R., Morgens, D.W., Vu, B.K., Kennedy, M.C., Han,
972 K., Li, A., Hess, G.T., Bassik, M.C., Chen, J.K., Nachury, M.V., 2018. A CRISPR-based
973 screen for Hedgehog signaling provides insights into ciliary function and ciliopathies.
974 Nat. Genet. 50, 460–471. https://doi.org/10.1038/s41588-018-0054-7
975
976 Chang, N., Sun, C., Gao, L., Zhu, D., Xu, X., Zhu, X., Xiong, J.-W., Xi, J.J., 2013. Genome
977 editing with RNA-guided Cas9 nuclease in Zebrafish embryos. Cell Res. 23, 465–472.
978 https://doi.org/10.1038/cr.2013.45
979
980 Choksi, S.P., Babu, D., Lau, D., Yu, X., Roy, S., 2014. Systematic discovery of novel ciliary
981 genes through functional genomics in the zebrafish. Development 141, 3410–3419.
982 https://doi.org/10.1242/dev.108209
983
984 Dickinson, D.J., Ward, J.D., Reiner, D.J., Goldstein, B., 2013. Engineering the Caenorhabditis

elegans genome using Cas9-triggered homologous recombination. Nat. Methods 10, 1028–1034. https://doi.org/10.1038/nmeth.2641

Evans, R.J., Schwarz, N., Nagel-Wolfrum, K., Wolfrum, U., Hardcastle, A.J., Cheetham, M.E., 2010. The retinitis pigmentosa protein RP2 links pericentriolar vesicle transport between the Golgi and the primary cilium. Hum. Mol. Genet. 19, 1358–1367. https://doi.org/10.1093/hmg/ddq012

Gabler, F., Nam, S., Till, S., Mirdita, M., Steinegger, M., Söding, J., Lupas, A.N., Alva, V., 2020. Protein Sequence Analysis Using the MPI Bioinformatics Toolkit. Curr. Protoc. Bioinforma. 72. https://doi.org/10.1002/cpbi.108

Herman, R.K., Hedgecock, E.M., 1990. Limitation of the size of the vulval primordium of Caenorhabditis elegans by lin-15 expression in surrounding hypodermis. Nature 348, 169–171. https://doi.org/10.1038/348169a0

Ivanova, A.A., East, M.P., Yi, S.L., Kahn, R.A., 2014. Characterization of Recombinant ELMOD (Cell Engulfment and Motility Domain) Proteins as GTPase-activating Proteins (GAPs) for ARF Family GTPases. J. Biol. Chem. 289, 11111–11121. https://doi.org/10.1074/jbc.M114.548529

Jaworek, T.J., Richard, E.M., Ivanova, A.A., Giese, A.P.J., Choo, D.I., Khan, S.N., Riazuddin, Sheikh, Kahn, R.A., Riazuddin, Saima, 2013. An Alteration in ELMOD3, an Arl2 GTPase-Activating Protein, Is Associated with Hearing Impairment in Humans. PLoS Genet. 9, e1003774. https://doi.org/10.1371/journal.pgen.1003774

Jensen, V.L., Carter, S., Sanders, A.A.W.M., Li, C., Kennedy, J., Timbers, T.A., Cai, J., Scheidel, N., Kennedy, B.N., Morin, R.D., Leroux, M.R., Blacque, O.E., 2016. Whole-Organism Developmental Expression Profiling Identifies RAB-28 as a Novel Ciliary GTPase Associated with the BBSome and Intraflagellar Transport. PLOS Genet. 12, e1006469. https://doi.org/10.1371/journal.pgen.1006469

Jensen, V.L., Lambacher, N.J., Li, C., Mohan, S., Williams, C.L., Inglis, P.N., Yoder, B.K., Blacque, O.E., Leroux, M.R., 2018. Role for intraflagellar transport in building a functional transition zone. EMBO Rep. 19. https://doi.org/10.15252/embr.201845862

Jin, H., White, S.R., Shida, T., Schulz, S., Aguiar, M., Gygi, S.P., Bazan, J.F., Nachury, M.V., 2010. The Conserved Bardet-Biedl Syndrome Proteins Assemble a Coat that Traffics Membrane Proteins to Cilia. Cell 141, 1208–1219. https://doi.org/10.1016/j.cell.2010.05.015

Johnson, K.R., Longo-Guess, C.M., Gagnon, L.H., 2012. Mutations of the Mouse ELMO Domain Containing 1 Gene (Elmod1) Link Small GTPase Signaling to Actin Cytoskeleton Dynamics in Hair Cell Stereocilia. PLoS ONE 7, e36074. https://doi.org/10.1371/journal.pone.0036074

Kaplan, O.I., Doroquez, D.B., Cevik, S., Bowie, R.V., Clarke, L., Sanders, A.A.W.M., Kida, K., Rappoport, J.Z., Sengupta, P., Blacque, O.E., 2012. Endocytosis Genes Facilitate Protein and Membrane Transport in C. elegans Sensory Cilia. Curr. Biol. 22, 451–460. https://doi.org/10.1016/j.cub.2012.01.060

Lambacher, N.J., Bruel, A.-L., van Dam, T.J.P., Szymańska, K., Slaats, G.G., Kuhns, S., McManus, G.J., Kennedy, J.E., Gaff, K., Wu, K.M., van der Lee, R., Burglen, L., Doummar, D., Rivière, J.-B., Faivre, L., Attié-Bitach, T., Saunier, S., Curd, A., Peckham, M., Giles, R.H., Johnson, C.A., Huynen, M.A., Thauvin-Robinet, C., Blacque, O.E., 2016. TMEM107 recruits ciliopathy proteins to subdomains of the ciliary transition zone and causes Joubert syndrome. Nat. Cell Biol. 18, 122–131. https://doi.org/10.1038/ncb3273

Lechtreck, K.-F., Johnson, E.C., Sakai, T., Cochran, D., Ballif, B.A., Rush, J., Pazour, G.J., Ikebe, M., Witman, G.B., 2009. The Chlamydomonas reinhardtii BBSome is an IFT cargo required for export of specific signaling proteins from flagella. J. Cell Biol. 187, 1117–1132. https://doi.org/10.1083/jcb.200909183

Lee, E., Sivan-Loukianova, E., Eberl, D.F., Kernan, M.J., 2008. An IFT-A protein is required to delimit functionally distinct zones in mechanosensory cilia. Curr. Biol. CB 18, 1899–1906. https://doi.org/10.1016/j.cub.2008.11.020

Li, J.B., Gerdes, J.M., Haycraft, C.J., Fan, Y., Teslovich, T.M., May-Simera, H., Li, H., Blacque, O.E., Li, L., Leitch, C.C., Lewis, R.A., Green, J.S., Parfrey, P.S., Leroux, M.R., Davidson, W.S., Beales, P.L., Guay-Woodford, L.M., Yoder, B.K., Stormo, G.D., Katsanis, N., Dutcher, S.K., 2004. Comparative Genomics Identifies a Flagellar and Basal Body Proteome that Includes the BBS5 Human Disease Gene. Cell 117, 541–552. https://doi.org/10.1016/S0092-8674(04)00450-7

Liem, K.F., Ashe, A., He, M., Satir, P., Moran, J., Beier, D., Wicking, C., Anderson, K.V., 2012. The IFT-A complex regulates Shh signaling through cilia structure and membrane protein trafficking. J. Cell Biol. 197, 789–800. https://doi.org/10.1083/jcb.201110049

Loktev, A.V., Zhang, Q., Beck, J.S., Searby, C.C., Scheetz, T.E., Bazan, J.F., Slusarski, D.C., Sheffield, V.C., Jackson, P.K., Nachury, M.V., 2008. A BBSome Subunit Links Ciliogenesis, Microtubule Stability, and Acetylation. Dev. Cell 15, 854–865. https://doi.org/10.1016/j.devcel.2008.11.001

Mangeol, P., Prevo, B., Peterman, E.J.G., 2016. KymographClear and KymographDirect: two tools for the automated quantitative analysis of molecular and cellular dynamics using kymographs. Mol. Biol. Cell 27, 1948–1957. https://doi.org/10.1091/mbc.E15-06-0404

Mick, D.U., Rodrigues, R.B., Leib, R.D., Adams, C.M., Chien, A.S., Gygi, S.P., Nachury, M.V., 2015. Proteomics of Primary Cilia by Proximity Labeling. Dev. Cell 35, 497–512.

https://doi.org/10.1016/j.devcel.2015.10.015

Miryounesi, M., Bahari, S., Salehpour, S., Alipour, N., Ghafouri-Fard, S., 2019. ELMO Domain Containing 1 (ELMOD1) Gene Mutation Is Associated with Mental Retardation and Autism Spectrum Disorder. J. Mol. Neurosci. 69, 312–315. https://doi.org/10.1007/s12031-019-01359-z

Mukhopadhyay, S., Wen, X., Chih, B., Nelson, C.D., Lane, W.S., Scales, S.J., Jackson, P.K., 2010. TULP3 bridges the IFT-A complex and membrane phosphoinositides to promote trafficking of G protein-coupled receptors into primary cilia. Genes Dev. 24, 2180–2193. https://doi.org/10.1101/gad.1966210

Nachury, M.V., 2014. How do cilia organize signalling cascades? Philos. Trans. R. Soc. Lond. B. Biol. Sci. 369. https://doi.org/10.1098/rstb.2013.0465

Nachury, M.V., Loktev, A.V., Zhang, Q., Westlake, C.J., Peränen, J., Merdes, A., Slusarski, D.C., Scheller, R.H., Bazan, J.F., Sheffield, V.C., Jackson, P.K., 2007. A Core Complex of BBS Proteins Cooperates with the GTPase Rab8 to Promote Ciliary Membrane Biogenesis. Cell 129, 1201–1213. https://doi.org/10.1016/j.cell.2007.03.053

Nozaki, S., Castro Araya, R.F., Katoh, Y., Nakayama, K., 2019. Requirement of IFT-B–BBSome complex interaction in export of GPR161 from cilia. Biol. Open 8, bio043786. https://doi.org/10.1242/bio.043786

Ou, G., E. Blacque, O., Snow, J.J., Leroux, M.R., Scholey, J.M., 2005. Functional coordination of intraflagellar transport motors. Nature 436, 583–587. https://doi.org/10.1038/nature03818

Ou, G., Koga, M., Blacque, O.E., Murayama, T., Ohshima, Y., Schafer, J.C., Li, C., Yoder, B.K., Leroux, M.R., Scholey, J.M., 2007. Sensory Ciliogenesis in *Caenorhabditis elegans* : Assignment of IFT Components into Distinct Modules Based on Transport and Phenotypic Profiles. Mol. Biol. Cell 18, 1554–1569. https://doi.org/10.1091/mbc.e06-09-0805

Patel-King, R.S., Gilberti, R.M., Hom, E.F.Y., King, S.M., 2013. WD60/FAP163 is a dynein intermediate chain required for retrograde intraflagellar transport in cilia. Mol. Biol. Cell 24, 2668–2677. https://doi.org/10.1091/mbc.E13-05-0266

Pazour, G.J., Dickert, B.L., Vucica, Y., Seeley, E.S., Rosenbaum, J.L., Witman, G.B., Cole, D.G., 2000. Chlamydomonas IFT88 and its mouse homologue, polycystic kidney disease gene tg737, are required for assembly of cilia and flagella. J. Cell Biol. 151, 709–718. https://doi.org/10.1083/jcb.151.3.709

Piasecki, B.P., Burghoorn, J., Swoboda, P., 2010. Regulatory Factor X (RFX)-mediated transcriptional rewiring of ciliary genes in animals. Proc. Natl. Acad. Sci. 107, 12969–12974. https://doi.org/10.1073/pnas.0914241107

Prevo, B., Scholey, J.M., Peterman, E.J.G., 2017. Intraflagellar transport: mechanisms of motor action, cooperation, and cargo delivery. FEBS J. 284, 2905–2931. https://doi.org/10.1111/febs.14068

Reiter, J.F., Leroux, M.R., 2017. Genes and molecular pathways underpinning ciliopathies. Nat. Rev. Mol. Cell Biol. 18, 533–547. https://doi.org/10.1038/nrm.2017.60

Rompolas, P., Pedersen, L.B., Patel-King, R.S., King, S.M., 2007. *Chlamydomonas* FAP133 is a dynein intermediate chain associated with the retrograde intraflagellar transport motor. J. Cell Sci. 120, 3653–3665. https://doi.org/10.1242/jcs.012773

Rosenbaum, J.L., Witman, G.B., 2002. Intraflagellar transport. Nat. Rev. Mol. Cell Biol. 3, 813–825. https://doi.org/10.1038/nrm952

Ruiz García, S., Deprez, M., Lebrigand, K., Cavard, A., Paquet, A., Arguel, M.-J., Magnone, V., Truchi, M., Caballero, I., Leroy, S., Marquette, C.-H., Marcet, B., Barbry, P., Zaragosi, L.-E., 2019. Novel dynamics of human mucociliary differentiation revealed by single-cell RNA sequencing of nasal epithelial cultures. Development dev.177428. https://doi.org/10.1242/dev.177428

Satir, P., Christensen, S.T., 2007. Overview of Structure and Function of Mammalian Cilia. Annu. Rev. Physiol. 69, 377–400. https://doi.org/10.1146/annurev.physiol.69.040705.141236

Saudi Mendeliome Group, 2015. Comprehensive gene panels provide advantages over clinical exome sequencing for Mendelian diseases. Genome Biol. 16, 134. https://doi.org/10.1186/s13059-015-0693-2

Scheidel, N., Blacque, O.E., 2018. Intraflagellar Transport Complex A Genes Differentially Regulate Cilium Formation and Transition Zone Gating. Curr. Biol. 28, 3279-3287.e2. https://doi.org/10.1016/j.cub.2018.08.017

Schneider, C.A., Rasband, W.S., Eliceiri, K.W., 2012. NIH Image to ImageJ: 25 years of image analysis. Nat. Methods 9, 671–675. https://doi.org/10.1038/nmeth.2089

Scholey, J., 2007. The sensory cilia of Caenorhabditis elegans_Revised. WormBook. https://doi.org/10.1895/wormbook.1.126.2

Schwarz, N., Lane, A., Jovanovic, K., Parfitt, D.A., Aguila, M., Thompson, C.L., da Cruz, L., Coffey, P.J., Chapple, J.P., Hardcastle, A.J., Cheetham, M.E., 2017. Arl3 and RP2 regulate the trafficking of ciliary tip kinesins. Hum. Mol. Genet. 26, 2480–2492. https://doi.org/10.1093/hmg/ddx143

Shaheen, R., Szymanska, K., Basu, B., Patel, N., Ewida, N., Faqeih, E., Al Hashem, A., Derar,

N., Alsharif, H., Aldahmesh, M.A., Alazami, A.M., Hashem, M., Ibrahim, N., Abdulwahab, F.M., Sonbul, R., Alkuraya, H., Alnemer, M., Al Tala, S., Al-Husain, M., Morsy, H., Seidahmed, M.Z., Meriki, N., Al-Owain, M., AlShahwan, S., Tabarki, B., Salih, M.A., Ciliopathy WorkingGroup, Faquih, T., El-Kalioby, M., Ueffing, M., Boldt, K., Logan, C.V., Parry, D.A., Al Tassan, N., Monies, D., Megarbane, A., Abouelhoda, M., Halees, A., Johnson, C.A., Alkuraya, F.S., 2016. Characterizing the morbid genome of ciliopathies. Genome Biol. 17, 242. https://doi.org/10.1186/s13059-016-1099-5

Shamseldin, H.E., Shaheen, R., Ewida, N., Bubshait, D.K., Alkuraya, H., Almardawi, E., Howaidi, A., Sabr, Y., Abdalla, E.M., Alfaifi, A.Y., Alghamdi, J.M., Alsagheir, A., Alfares, A., Morsy, H., Hussein, M.H., Al-Muhaizea, M.A., Shagrani, M., Al Sabban, E., Salih, M.A., Meriki, N., Khan, R., Almugbel, M., Qari, A., Tulba, M., Mahnashi, M., Alhazmi, K., Alsalamah, A.K., Nowilaty, S.R., Alhashem, A., Hashem, M., Abdulwahab, F., Ibrahim, N., Alshidi, T., AlObeid, E., Alenazi, M.M., Alzaidan, H., Rahbeeni, Z., Al-Owain, M., Sogaty, S., Seidahmed, M.Z., Alkuraya, F.S., 2020. The morbid genome of ciliopathies: an update. Genet. Med. Off. J. Am. Coll. Med. Genet. 22, 1051–1060. https://doi.org/10.1038/s41436-020-0761-1

Sigg, M.A., Menchen, T., Lee, C., Johnson, J., Jungnickel, M.K., Choksi, S.P., Garcia, G., Busengdal, H., Dougherty, G.W., Pennekamp, P., Werner, C., Rentzsch, F., Florman, H.M., Krogan, N., Wallingford, J.B., Omran, H., Reiter, J.F., 2017. Evolutionary Proteomics Uncovers Ancient Associations of Cilia with Signaling Pathways. Dev. Cell 43, 744-762.e11. https://doi.org/10.1016/j.devcel.2017.11.014

Silflow, C.D., Lefebvre, P.A., 2001. Assembly and Motility of Eukaryotic Cilia and Flagella. Lessons from *Chlamydomonas reinhardtii*. Plant Physiol. 127, 1500–1507. https://doi.org/10.1104/pp.010807

Sleigh, M.A., 1989. Adaptations of ciliary systems for the propulsion of water and mucus. Comp. Biochem. Physiol. A Physiol. 94, 359–364. https://doi.org/10.1016/0300-9629(89)90559-8

SYSCILIA Study Group, van Dam, T.J., Wheway, G., Slaats, G.G., Huynen, M.A., Giles, R.H., 2013. The SYSCILIA gold standard (SCGSv1) of known ciliary components and its applications within a systems biology consortium. Cilia 2, 7. https://doi.org/10.1186/2046-2530-2-7

Thisse, B., Heyer, V., Lux, A., Alunni, V., Degrave, A., Seiliez, I., Kirchner, J., Parkhill, J.-P., Thisse, C., 2004. Spatial and Temporal Expression of the Zebrafish Genome by Large-Scale In Situ Hybridization Screening, in: Methods in Cell Biology. Elsevier, pp. 505–519. https://doi.org/10.1016/S0091-679X(04)77027-2

Turn, R.E., Linnert, J., Gigante, E.D., Wolfrum, U., Caspary, T., Kahn, R.A., 2021. Roles for ELMOD2 and Rootletin in ciliogenesis. Mol. Biol. Cell 32, 800–822. https://doi.org/10.1091/mbc.E20-10-0635

Turan MG, Kantarci H, Temtek SD, Cakici O, Cevik S, Kaplan OI. 2022., Protocol for determining the average speed and frequency of kinesin and dynein-driven intraflagellar transport (IFT) in C. elegans. STAR Protoc;3(3):101498. doi: 10.1016/j.xpro.2022.101498.

UK10K Rare Diseases Group, Boldt, K., van Reeuwijk, J., Lu, Q., Koutroumpas, K., Nguyen, T.-M.T., Texier, Y., van Beersum, S.E.C., Horn, N., Willer, J.R., Mans, D.A., Dougherty, G., Lamers, I.J.C., Coene, K.L.M., Arts, H.H., Betts, M.J., Beyer, T., Bolat, E., Gloeckner, C.J., Haidari, K., Hetterschijt, L., Iaconis, D., Jenkins, D., Klose, F., Knapp, B., Latour, B., Letteboer, S.J.F., Marcelis, C.L., Mitic, D., Morleo, M., Oud, M.M., Riemersma, M., Rix, S., Terhal, P.A., Toedt, G., van Dam, T.J.P., de Vrieze, E., Wissinger, Y., Wu, K.M., Apic, G., Beales, P.L., Blacque, O.E., Gibson, T.J., Huynen, M.A., Katsanis, N., Kremer, H., Omran, H., van Wijk, E., Wolfrum, U., Kepes, F., Davis, E.E., Franco, B., Giles, R.H., Ueffing, M., Russell, R.B., Roepman, R., 2016. An organelle-specific protein landscape identifies novel diseases and molecular mechanisms. Nat. Commun. 7, 11491. https://doi.org/10.1038/ncomms11491

van Dam, T.J.P., Kennedy, J., van der Lee, R., de Vrieze, E., Wunderlich, K.A., Rix, S., Dougherty, G.W., Lambacher, N.J., Li, C., Jensen, V.L., Leroux, M.R., Hjeij, R., Horn, N., Texier, Y., Wissinger, Y., van Reeuwijk, J., Wheway, G., Knapp, B., Scheel, J.F., Franco, B., Mans, D.A., van Wijk, E., Képès, F., Slaats, G.G., Toedt, G., Kremer, H., Omran, H., Szymanska, K., Koutroumpas, K., Ueffing, M., Nguyen, T.-M.T., Letteboer, S.J.F., Oud, M.M., van Beersum, S.E.C., Schmidts, M., Beales, P.L., Lu, Q., Giles, R.H., Szklarczyk, R., Russell, R.B., Gibson, T.J., Johnson, C.A., Blacque, O.E., Wolfrum, U., Boldt, K., Roepman, R., Hernandez-Hernandez, V., Huynen, M.A., 2019. CiliaCarta: An integrated and validated compendium of ciliary genes. PLOS ONE 14, e0216705. https://doi.org/10.1371/journal.pone.0216705

Vasquez SSV, van Dam J, Wheway G. 2021. An updated SYSCILIA gold standard (SCGSv2) of known ciliary genes, revealing the vast progress that has been made in the cilia research field. Mol Biol Cell. 2021 Dec 1;32(22):br13. doi: 10.1091/mbc.E21-05-0226.

Wei, Q., Xu, Q., Zhang, Y., Li, Y., Zhang, Q., Hu, Z., Harris, P.C., Torres, V.E., Ling, K., Hu, J., 2013. Transition fibre protein FBF1 is required for the ciliary entry of assembled intraflagellar transport complexes. Nat. Commun. 4, 2750. https://doi.org/10.1038/ncomms3750

Wei, Q., Zhang, Y., Li, Y., Zhang, Q., Ling, K., Hu, J., 2012. The BBSome controls IFT assembly and turnaround in cilia. Nat. Cell Biol. 14, 950–957. https://doi.org/10.1038/ncb2560

Wheway, G., Genomics England Research Consortium, Mitchison, H.M., 2019. Opportunities and Challenges for Molecular Understanding of Ciliopathies–The 100,000 Genomes Project. Front. Genet. 10, 127. https://doi.org/10.3389/fgene.2019.00127

Williams, C.L., Li, C., Kida, K., Inglis, P.N., Mohan, S., Semenec, L., Bialas, N.J., Stupay,

R.M., Chen, N., Blacque, O.E., Yoder, B.K., Leroux, M.R., 2011. MKS and NPHP modules cooperate to establish basal body/transition zone membrane associations and ciliary gate function during ciliogenesis. J. Cell Biol. 192, 1023–1041. https://doi.org/10.1083/jcb.201012116

Williams, C.L., McIntyre, J.C., Norris, S.R., Jenkins, P.M., Zhang, L., Pei, Q., Verhey, K., Martens, J.R., 2014. Direct evidence for BBSome-associated intraflagellar transport reveals distinct properties of native mammalian cilia. Nat. Commun. 5, 5813. https://doi.org/10.1038/ncomms6813

Wright, K.J., Baye, L.M., Olivier-Mason, A., Mukhopadhyay, S., Sang, L., Kwong, M., Wang, W., Pretorius, P.R., Sheffield, V.C., Sengupta, P., Slusarski, D.C., Jackson, P.K., 2011. An ARL3-UNC119-RP2 GTPase cycle targets myristoylated NPHP3 to the primary cilium. Genes Dev. 25, 2347–2360. https://doi.org/10.1101/gad.173443.111

Xu, Q., Zhang, Y., Wei, Q., Huang, Y., Li, Y., Ling, K., Hu, J., 2015. BBS4 and BBS5 show functional redundancy in the BBSome to regulate the degradative sorting of ciliary sensory receptors. Sci. Rep. 5, 11855. https://doi.org/10.1038/srep11855

Xu, W., Jin, M., Hu, R., Wang, H., Zhang, F., Yuan, S., Cao, Y., 2017. The Joubert Syndrome Protein Inpp5e Controls Ciliogenesis by Regulating Phosphoinositides at the Apical Membrane. J. Am. Soc. Nephrol. 28, 118–129. https://doi.org/10.1681/ASN.2015080906

Ye, F., Nager, A.R., Nachury, M.V., 2018. BBSome trains remove activated GPCRs from cilia by enabling passage through the transition zone. J. Cell Biol. 217, 1847–1868. https://doi.org/10.1083/jcb.201709041